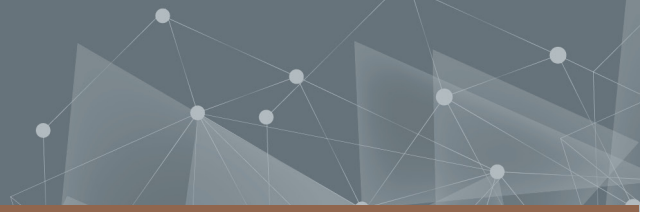




CHALMERS
UNIVERSITY OF TECHNOLOGY



Investigation on RANS prediction of propeller induced pressure pulses and sheet-tip cavitation interactions in Behind Hull Conditions

Master's thesis in Naval Architecture and Ocean Engineering

KELVIN ELO-OGHENE ELOHO

DEPARTMENT OF MECHANICS AND MARITIME SCIENCES

CHALMERS UNIVERSITY OF TECHNOLOGY

Gothenburg, Sweden 2022

www.chalmers.se

MASTER'S THESIS 2022

**Investigation on RANS prediction of
propeller induced pressure pulses and sheet-tip
cavitation interactions in Behind Hull Conditions**

KELVIN ELO-OGHENE ELOHO



CHALMERS
UNIVERSITY OF TECHNOLOGY

Department of Mechanics and Maritime Sciences
Division of Marine Technology
CHALMERS UNIVERSITY OF TECHNOLOGY
Gothenburg, Sweden 2022

Investigation on RANS prediction of propeller induced pressure pulses and
sheet-tip cavitation interactions in Behind Hull Conditions
KELVIN ELO-OGHENE ELOHO

© KELVIN ELO-OGHENE ELOHO, 2022.

Supervisor: Rickard Bensow, Department of Mechanics and Maritime Sci-
ences

Report number: 2022:01

Master's Thesis 2022
Department of Mechanics and Maritime Sciences
Division of Marine Technology
Chalmers University of Technology
SE-412 96 Gothenburg
Telephone +46 31 772 1000

Cover: Cavities detached of blade trailing edge visualised by STAR-CCM+.

Gothenburg, Sweden 2022

Investigation on RANS prediction of propeller induced pressure pulses and sheet-tip cavitation interactions in Behind Hull Conditions
KELVIN ELO-OGHENE ELOHO
Department of Mechanics and Maritime Sciences
Chalmers University of Technology

Abstract

Propeller blades' cavitation is not only a significant cause of Underwater radiated Noise (URN), but it is also detrimental to the propeller blades and ship engines due to resulting erosion and vibrations, respectively. Over the years, different approaches have been engaged to predict cavitation using viscous flow methodologies accurately. However, the practicalities of these methodologies have not been stamped.

Data from previous experiments in open-water, full and model scale are used for verification. Details of the experimental approach used are not included in this report. This thesis investigates propeller-induced pressure pulses and resulting cavitation providing visuals of the cavities formed corresponding to the pressure broadband spectra. In decades past, sheet cavitation has been predicted more often in comparison to tip-vortex cavitation. However, this thesis aims also to shed light on blade-tip cavitation, showing a detachment from sheet to vortex cavitation from the propeller blade trailing edge tip.

The upstream wake on which the propeller works is simulated from the provided ship hull. This is done by performing steady-state simulations. After which, transient simulations are performed. The transient simulations comprise the propeller's rotations in cavitating and non-cavitating conditions. The simulations aim to depict the real-life scenario by operating the propeller in behind-hull conditions. However, the free surface and resulting kelvin waves are neglected in this thesis.

The investigation analyses the accuracy of the approach used. Initially, the wake field is predicted after which spectral analyses of the pressure pulses are performed and compared to the experimental. The cavitating pattern is also reviewed. The studies engaged in this report show the RANS methodology provide a accurate prediction of the propeller rotation phenomenon in non-cavitating conditions. However, the RANS approach requires a highly independent and fine mesh to make correct predictions in cavitating conditions. The power spectral densities predicted show disparities with the experimental result. However, an analogous visualization of cavitation is achieved. The predictions is highly dependent on the accurate ship-propeller wake prediction.

Keywords: cavitation, RANS, CFD, pressure pulses.

Acknowledgements

I want to show appreciation to my supervisor Professor Rickard E. Bensow. First of all, for his recurring patience. Even when this project overstayed its required duration, He kept supporting and providing guidance and feedback when required. Second, I am highly thankful to Muye Ge for his advice and aid. I returned bewildered occasionally, but he always offered assistance and guidance.

Great appreciation goes to my family (parents and sisters) for their tremendous support and unwavering belief in me.

The simulations performed were quickened by resources at Chalmers Centre for Computational Science and Engineering (C3SE).

Kelvin Elo-oghene Eloho, Gothenburg, December 2022

Contents

List of Figures	x <i>i</i>
List of Tables	x <i>ii</i>
Acronyms	x <i>iv</i>
Annotations	x <i>vi</i>
1 Introduction	1
1.1 Background	1
1.2 Problem Definition and Objectives	2
1.3 Delimitations and Limitations	3
1.4 Outline of Thesis	3
2 Methods	5
2.1 Governing Equations for fluid Flow	5
2.1.1 Continuity Equations	5
2.1.1.1 Modeling Turbulent Viscosity	6
2.1.1.2 Fluid Mixture Approach	7
2.2 Propeller blade cavitation dynamics	7
2.2.1 Bubble Dynamics	8
2.2.1.0.1 Rayleigh Plesset Equation:	8
2.2.2 Schnerr-Sauer model	8
2.2.3 Cavitation types	9
2.2.3.1 Vortex cavitation	10
2.2.3.2 Sheet Cavitation	11
2.3 Hull-propeller pressure fluctuations	11
2.3.1 Power Spectral Estimation	13
2.4 Separation and Gamma ReTheta Transition model	14
2.4.1 Separation	14
2.4.2 $\gamma - Re_{\theta t}$ model	14
2.5 STAR-CCM+	15
2.6 Simulation Setup	16
2.6.1 Case Description	16
2.6.2 Pre-processor	17
2.6.3 Simulations Outline	18

2.6.4	Mesh Setup	19
2.6.5	Solver details	19
3	Results	21
3.1	Model case and CFD uncertainty analyses	21
3.1.1	Propeller Models	21
3.1.2	Ship model	23
3.1.3	Solution Convergence and Thrust Coefficients	25
3.2	Wake Prediction	26
3.3	Hull Pressure pulses	26
3.3.1	Data Comparison	27
3.3.1.1	Analyses of Variance	28
3.4	Cavitating Pattern	32
4	Conclusion and Discussions	36
4.1	Validation and Verification of Methodology	36
4.1.1	Frequency Resolution	37
4.2	Cavitation and Hull-Pressure Fluctuations	37
5	Future Work	38
A	Appendix 1	I

List of Figures

2.1	Common Cavitation Patterns on Ship Propellers ITTC, 2002	10
2.2	Location of Pressure Transducers in both Experiment and CFD simulations	12
2.3	Sample of processed signal from a Cavitating propeller.	13
2.4	Domain	17
2.5	Simulations Outline	18
2.6	Mesh Overview	19
3.1	High skew propeller	21
3.2	Propeller Blade Grid	23
3.3	Cells near-field, $Q > 200$	23
3.4	Residuals	25
3.5	Ship to Propeller wake	26
3.6	Spectral Analyses Comparison	27
3.7	Spectral Analyses Comparison for Cavitating condition between CFD model and Experimental	29
3.8	Spectral Analyses Comparison for Cavitating condition between CFD model and Experimental (Sister case)	30
3.9	Spectral Analyses Comparison for Non-cavitating condition between CFD model and Experimental (Sister case)	30
3.10	Full Spectral Analysis of Probe 1 data	31
3.13	Cavitation comparison	32
3.11	Cavitation comparison	33
3.12	Cavitation comparison	34
3.14	Irrotationality at center of cavity	35
A.1	Spectral Analyses Comparison, Probe 2	I
A.2	Spectral Analyses Comparison, Probe 3	II
A.3	Spectral Analyses Comparison, Probe 4	II
A.4	Spectral Analyses Comparison, Probe 5	III
A.5	Spectral Analyses Comparison, Probe 6	III
A.6	Spectral Analyses Comparison, Probe 7	IV
A.7	Spectral Analyses Comparison, Probe 8	IV
A.8	Spectral Analyses Comparison, Probe 9	V
A.9	Spectral Analyses Comparison, Probe 10	V
A.10	Spectral Analyses Comparison, Probe 11	VI
A.11	Spectral Analyses Comparison, Probe 12	VI

A.12 Spectral Analyses Comparison, Probe 13	VII
A.13 Spectral Analyses Comparison, Probe 14	VII
A.14 Spectral Analyses Comparison, Probe 15	VIII
A.15 Spectral Analyses Comparison, Probe 16	VIII
A.16 Spectral Analyses Comparison, Probe 17	IX
A.17 Spectral Analyses Comparison, Probe 18	IX
A.18 Spectral Analyses Comparison, Probe 19	X
A.19 Spectral Analyses Comparison, Probe 20	X
A.20 Spectral Analyses Comparison, Probe 21	XI

List of Tables

2.1	Ship Hull full-scale properties	16
2.2	propeller properties	16
3.1	KT comparison (experimental value: 0.217)	25
3.2	Analyses of Variance of Sound Pressure Levels for cavitating conditions	28
3.3	Analyses of Variance of Sound Pressure Levels for non-cavitating conditions (CFD model against Experimental for sister case) .	28
3.4	Sample ANOVA for two data with same SPL	29

Acronyms

UN	United Nations
URN	Under-water Radiated Noise
CFD	Computational Fluid Dynamics
RANS	Reynolds Average Navier Stokes
LES	Large Eddy Simulation
BEM	Boundary Element Method
SST	Shear Stress Transport
VOF	Volume of Fluid
DWB	Depressurized Wave Basins
CAE	Computer Aided Engineering
SIMPLE	Semi-Implicit Method for Pressure-Linked Equations
MUSCL	Monotonic Upstream-centered Scheme for Conservation Laws
FT	Fourier Transform
BPF	Blade Passing Frequency
ILU	Incomplete Lower-Upper
MRF	Moving Reference Frame
PISO	Pressure-Implicit with Splitting of Operators
RBM	Rotating Body Motion
LOA	Length Overall
LOA	Analysis of Variance
CAE	Computer-aided engineering
MUSCL	Monotonic Upstream-centered Scheme for Conservation Laws
KTE	Kinetic Turbulent Energy
SDr	Specific Dissipation Rate
Lpp	Length between perpendiculars
SPL	Sound Pressure Level
PSD	Power Spectral Density
'l'	Liquid phase
'v'	Vapour phase
ITTC	International Towing Tank Conference

Annotations

D	Diameter [m]
E_γ	Destructive/laminarization source term []
Fr	Froude number []
H	Shape factor
J	Advance Ratio []
KQ	Propeller Torque Coefficient []
KT	Propeller Thrust coefficient []
LOA	Length Over All [m]
L_{PP}	Length between perpendiculars [m]
P_γ	Production term
Q	Torque [$N - m$]
R	Radius [m]
$S(f)$	Energy across Frequency domain [J]
S_{ij}	Strain-rate tensor
T	Thrust [N]
U_∞	Flow velocity in domain [m/s]
V_∞	Inlet velocity [m/s]
Vol	Volume [m^3]
WL	Waterline [m]
Ω	Anti-symmetric/vorticity tensor
γ	Intermittency
μ	Dynamic Viscosity [$Pa - s$]
μ_t	Turbulent viscosity [m^2/s]
ω	Magnitude of Strain rate []
ψ_ω	Destructive term []
ρ	Density [kg/m^3]
σ	Cavitation number
τ	Shear Stress [Pa]
$\tilde{Re}_{\theta t}$	Momentum thickness Reynolds number
\tilde{Re}	Reynolds number
f	Frequency [Hz]
m	Mass [kg]
n	Rotation speed [rps]
p_s	Saturation Pressure [Pa]
$p_{\infty t}$	Pressure across domain [Pa]
p_{ref}	Reference pressure [N/m^2]

$s(t)$	Energy across time domain [J]
t	Time [s]
u	Velocity in x direction [m]
v	Velocity [m/s]
v_r	Growth rate [m/s]
x	Length along longitudinals [m]
y	Length in transverse direction [m]

1

Introduction

1.1 Background

Whether it is trade, warfare, exploration or leisure, the need for ships can not be over-emphasized. '*Maritime transportation is the backbone of global trade and the global economy*' - UN Secretary-General Ban Ki-moon's message on World Maritime Day, 2016. The need for maritime transportation stresses the importance of ships in today's world.

Noise generation by ships seems to take off some of the beauty radiated by these grandiose watercraft. The exigency for minimal noise generation is now much felt, especially in maritime transportation's luxury and military sect. Over the last 30 years, noise generated by ships has increased exponentially. Ship generated noise is detrimental not only on-board the ships by a decrease in comfort levels experienced by passengers and crews but also inimical to sea life. Underwater Radiated Noise (URN) effects are harmful and disturbing to sea mammals (Erbe, 2011). Unlike light, sound is emitted better in large water bodies. Marine mammals depend on sound for communication and navigation. The effect of noise levels with acoustic characteristics mostly common to cavitating blades takes tolls on the life of marine mammals dependent on sound for essential activities. Broadband noise of over 100 to thousands of hertz is most often recorded at high ship speeds due to propeller cavitation and flow around the underwater part of the ship (Kozaczka and Grelowska, 2004). "*Cavitation of marine propellers is the most prevalent source of underwater sound in the oceans*" Ross, 1976.

Other deterring effects that can be attributed to cavitating propeller blades include ship vibrations. At the occurrence of cavitation, the pressure fluctuations results to vibration of connecting structures which is transmitted across the ship. The broadband excitation resultant can resonate with ship structures and is therefore detrimental. Cavitation also causes degradation of propeller blades surfaces. As the cavities collapse in hordes and are transferred across the blade surface as the flow progresses, material erosion takes place.

1.2 Problem Definition and Objectives

This investigation aims to predict pressure pulses induced by the propeller. It considers the resulting sheet and tip cavitation on the propeller cases being investigated. This thesis does not present ways to curb and reduce the resulting cavitation due to these pulses. The thesis is aimed to provide a meticulous prediction of pressure pulses induced by the propeller in play.

As earlier stated, noise levels are of great concern. Therefore, analysing the resulting pressure distribution on the hull above the propeller is incredibly beneficial to predicting these level. Furthermore, not only does the propeller's operation behind the hull result in noise production, but it also affects the resistance and propeller loading (Rijpkema et al., 2013). This just adds more reasons why precise analyses will be greatly beneficial.

Such predictions in recent years have been engaged by using a viscous flow CFD approach. Stern et al., 1988 list different approaches with empirical methods for predicting propeller cavitation noise. However, this research engages this problem using a RANS approach with the predefined methodology. Computational procedures for RANS can also be used in LES, such as pressure correction schemes like SIMPLE (Davidson et al., 2020). For example, the solution of a flow field using the pressure poisson equation or SIMPLE method could follow this order in both LES and RANS. First, solve the discretised Navier-Stokes equation for velocity vector \bar{v}_i . Establish an intermediate velocity field \bar{v}^*_i . Linear Interpolate to get the intermediate velocity field on the faces. Solve the poisson equation for pressure or SIMPLE equation for pressure with a multigrid method. Compute face velocities from intermediate velocities and pressure (satisfying continuity). Reiterate till convergence is achieved. Then compute turbulence viscosity. Before, next time step is engaged.

Turbulence models are also simpler in LES. However, the computational cost with LES is colossal. Therefore, in order to capture this minute scale turbulence using LES, higher quality mesh should be used. This why LES is good for flows that are governed by large turbulent structures. So, in situations where the boundary layer is attached, LES will give poor results except with finer mesh. The Direct Numerical Solutions (DNS) is also an accurate option. However, the use of DNS comes with a higher cost. DNS is basically more cells, better solution. For near-field resolution, using DNS will incur a lot more cells if compared to the RANS approach. Through the years, there have been improvements in propeller pressure pulses and cavitation predictions using various methodologies—for example, the use of the Boundary-Element Method (BEM) by Bosschers, 2018. However, the BEM's accuracy is questionable compared to the RANS approach.

In a nutshell, the objectives include:

- Predict the pressure pulse induced by the propeller on the hull.
- Check the interaction of the propeller with the formed jet within the ship wake profile.

- Analyse cavitation pattern (sheet and tip-vortex) and interactions.

These investigations will be done on two hull and propeller models. The resulting data will be compared with the experimental data acquired from the model test of one of the cases provided.

1.3 Delimitations and Limitations

The scope of this thesis is checked to a certain extent by various characteristics. Most of these boundaries are set by the limitations in this thesis. The work in this thesis is limited by various factors. Crowned are its resources as a master's thesis. It ends up investigating one case model. The case model being investigated possesses limited experimental data for validation. Therefore, unavailable data for validation will be compared to that of the sister case (sister ship and propeller). Correspondingly, discrepancies are expected as the experimental data of the two cases are somewhat different. For example, the thrust coefficients (KT) for both cases differ at design advance speed. The KT value for case 1 (not being analysed) is approximately 0.19, and the analysed case (case 2) is 0.217. The positions of the pressure transducers implemented on the numerical model case are akin to those on the experiment, which is set up for case 1. The minute differences in hull and propeller shape topography will affect the paralleling of the resulting data. However, some data are available for the case that is analysed, such as KT value and thrust coefficients.

Secondly, experiments at varying speeds and design drafts are not performed for this case being investigated.

The temperatures at which some experiments are performed are not specified. Therefore, the saturation pressure, viscosity and density can not be banked on to be accurate values.

The free surface wake is also neglected due to the resulting complexity in the numerical model if included. This could be put in future work. The free surface is then described as a symmetry boundary, i.e. zero scalar flux. Neglecting the influence of the ship waves.

Blockage and sidewall effects corrections are also not considered. This means tank boundary effects are not adequately identified to implement in the towing tank. Studies of blockage effects can be found in Guo et al., 2019.

This thesis does not suggest ways to curb or reduce the predicted cavitation. This report describes the resulting cavitation and pressure pulses. It does not present a mesh independence study but describes the grid utilised.

1.4 Outline of Thesis

The thesis is structured so that it narrates the basic information, method, results, and conclusions. It is split into four sections.

Chapter 1 gives information about the background of the thesis and the objectives.

Chapter 2 presents the methodology used, the basic equations, turbulence and transfer models. It also presents some theories about cavitation and the resulting noise.

Chapter 3 provides the results of the simulations performed on the cases provided. It presents the comparison of these results to the experimental results. In chapters 4 and 5, discussions about the accuracy of the results are provided, conclusions and future work are stated. The accuracy of the methodology is examined. Finally, a conclusion is provided, and future studies stated.

2

Methods

2.1 Governing Equations for fluid Flow

Before diving into elemental mass and momentum continuity equations of flow which are RANS systems of mean flow equations, the terminology 'RANS' is briefly outlined. Primal, RANS (Reynolds-averaged Navier–Stokes) equations describe turbulent flows. The pivots of RANS equations are the mean flow and the effects of turbulence on mean flow properties such as pressure, velocities and stresses (Versteeg and Malalasekera, 2007). The physical quantities at different instances of time are segregated into fluctuating and time-averaged properties (mean flow properties). However, the influence of turbulence on mean flows has to be analysed. Using RANS equations to predict flow turbulence will require the utilization of turbulence models to predict transport terms, Reynolds stresses and compute the mean flow equations for fluid flow (continuity and momentum equations).

2.1.1 Continuity Equations

The mass conservation and momentum equations for any incompressible flow are the fundamentals for fluid flow. Generally, the behaviour of properties of the flow will be presented as derivatives of time and space. For mass conservation, the mass flow rate into the continuum should be equivalent to the rate at which the mass in that continuum increases,

$$\dot{\rho} + \text{div}(\rho v_i) = 0 \quad (2.1)$$

Due to the incompressibility of the flow,

$$\frac{\partial v_i}{\partial x_i} = 0. \quad (2.2)$$

Using an Eulerian approach, which involves consideration of a fixed point (or unit area/volume) in space, the momentum transport equation (for Newtonian Viscous flow):

$$\rho \frac{\partial v_i}{\partial t} = - \frac{\partial p}{\partial x_i} + \frac{\partial \tau_{ji}}{\partial x_j} + \rho f_i. \quad (2.3)$$

Modelling the stress tensor τ_{ji} Ekh, 2017:

$$\tau_{ji} = 2\mu_t S_{ij} - \frac{2}{3}\mu \frac{\partial v_k}{\partial x_k} \delta_{ij}, \quad (2.4)$$

where μ represents the dynamic viscosity. S_{ij} is strain rate described as $S_{ij} = \frac{\partial v_i}{\partial x_j} + \frac{\partial v_j}{\partial x_i}$.

However, the Boussinesq hypothesis is used to model Reynolds stress tensor. In addition, when the mean velocity equals zero (still flow), the hydrodynamic pressure will also equate to zero. So,

$$\tau_{ij} = \rho_o \bar{v}_i \bar{v}_j. \quad (2.5)$$

Typically, the velocity v_i sums \bar{v}_i and v_i' i.e. $v_i = \bar{v}_i + v_i'$. \bar{v}_i represents mean velocity while v_i' represents fluctuating velocity. The momentum equation 2.3 can then be modified to be,

$$\frac{\partial \rho \bar{v}_i}{\partial t} = -\frac{\partial \bar{p}}{\partial x_i} + \mu \frac{\partial^2 \bar{v}_i}{\partial x_j \partial x_j} + f_i, \quad (2.6)$$

where, the partial differential of eqn 2.5 i.e. $\frac{\partial \tau_{ij}}{\partial x_j} = \frac{\partial}{\partial x_j} (\frac{\partial v_i}{\partial x_j} + \frac{\partial v_j}{\partial x_i})$. So,

$$\frac{\partial}{\partial x_j} (\frac{\partial v_i}{\partial x_j} + \frac{\partial v_j}{\partial x_i}) = \mu \frac{\partial^2 \bar{v}_i}{\partial x_j \partial x_j}. \quad (2.7)$$

In the equations above, f_i represents body force. \bar{p} represents the hydrodynamic pressure. μ_t is taken as the turbulent viscosity (described in section 2.1.1.1).

2.1.1.1 Modeling Turbulent Viscosity

The turbulent viscosity, μ_t is modelled using the Menter shear stress transport (SST) $k - \omega$ model. To suffice for the deficiencies of the $k - \epsilon$ and $k - \omega$ models. The eddy-viscosity model Menter SST $k - \omega$ utilises features from both the $k - \omega$ in the inner boundary layer (near-wall region) and $k - \epsilon$ at the outer (fully-turbulent) region of the boundary layer (Davidson et al., 2020).

The transformation of the $k - \epsilon$ model to the $k - \omega$ by the relation $\omega = \epsilon/(\beta^*k)$. $\beta^* = c_\mu$ (Davidson et al., 2020).

$$C_\omega = P_\omega + \psi_\omega + D_\omega^T + D_\omega^V \quad (2.8)$$

C_ω = convective term, P_ω is the production term, ψ_ω is the destructive term; D_ω^T represents the turbulent diffusion; and D_ω^V represents the viscous diffusion (Menter, 1992).

2.1.1.2 Fluid Mixture Approach

The cavitation phenomenon is portrayed by the switch of water from its liquid to its vapour phase. In order to properly depict this, the homogenous mixture approach is used. This is an approach that defines the liquid and vapour contents in single cells in the domain as uniform. The homogenous mixture approach treats the two-phased fluid as a mixture characterised by uniform properties of the liquid and vapour phases. The fluid is assumed to be immiscible and isothermal. Below are constitutive relations for the 2 phases for density ρ and viscosity μ .

$$\rho = \alpha_l \rho_l + (1 - \alpha_l) \rho_v \quad (2.9)$$

$$\mu = \alpha_l \mu_l + (1 - \alpha_l) \mu_v \quad (2.10)$$

where, α is the volume fraction and the subscripts l and v represent liquid and vapour phases. ρ_l and ρ_v represent densities of water in liquid and vapour phases respectively. i.e.

$$1 = \alpha_l + \alpha_v \quad (2.11)$$

$$\frac{\partial}{\partial t}(\alpha_l \rho_l + \rho_v - \alpha_l \rho_v) + \nabla \cdot \alpha_l v_i = 0 \quad (2.12)$$

$$\frac{\partial \alpha_l}{\partial t} + \nabla \cdot (\alpha_l v_i) = 0 \quad (2.13)$$

For cavitation mass transfer modelling, the Schnerr-Sauer model is utilised. This will be discussed in section 2.2.2. The transport equation of the liquid fractions governs the mass transfer across these phases. i.e.

$$\rho_l \frac{\partial}{\partial t} \alpha_l + \rho_l \nabla \cdot (\alpha_l v_i) = \dot{m} \quad (2.14)$$

\dot{m} sums both the creation of liquid phase from condensation and also its destruction due to vaporisation.

2.2 Propeller blade cavitation dynamics

A liquid can rupture in two different ways, by increasing temperature or pressure decrease. The rupture of the liquid by the increase in temperature at constant pressure is called boiling. While, the rupture of the liquid by pressure decrease to values below the vapour pressure of the liquid and constant temperature can be referred to as cavitation (Brennen, 2014).

Cavitation on propellers is heterogeneous nucleation. Rupture occurs due to significant interactions resultant from the motion of the propeller at the boundary of the blades' surface and water. To sum up, in a definition, cavitation is heterogeneous nucleation of a liquid caused by the decrease of pressure below vapour pressure resulting in the growth, then collapse of the liquid bubbles.

Cavitation happens when the pressure on the liquid goes below the critical

pressures $p_v - 2S/R$ (Brennen, 2014), where R is the radius of the liquid bubble and S is the tensile strength. When cavitation stems from the blade vortices, it could be labelled Vortex Cavitation (further explained in section 2.2.3.1). In addition, a separation zone of low pressure can be formed at even slight angles of attack, resulting in cavities formation. This is called sheet cavitation (further explained in section 2.2.3.2). In other to model the cavitation, i.e. the growth and collapse of bubbles and the convection of the fluid in the vapour phase, the Schnerr-Sauer model comes in handy.

2.2.1 Bubble Dynamics

Understanding the behaviour of the bubble in an infinite domain can put some light on the production of hull pressure pulses and noise due to the production and destruction of energy during growth and collapses.

2.2.1.0.1 Rayleigh Plesset Equation: Rayleigh, 1917 derived a relation that explains the pressure developed at the collapse of a bubble.

Let us consider a bubble in an infinite domain of Newtonian fluid at constant temperature and density. The bubble of radius R and its contents are of uniform temperature and pressure. The Reyleigh Plesset equation will be presented as:

$$\frac{p_B(t) - p_\infty(t)}{\rho_L} = R \frac{d^2 R}{dt^2} + \frac{3}{2} \left(\frac{dR}{dt} \right)^2 + \frac{2S}{\rho_L R} + \frac{4v_L}{R} \frac{dR}{dt} \quad (2.15)$$

Where, t represent quantities at a specific time. $p_B(t)$ is the pressure of the vapour in the bubble, p_∞ is the pressure of the fluid domain. ρ_L is the fluid density. S is the surface tension. R is the radius of the bubble. v_L is the dynamic viscosity of the fluid. (Brennen, 2014) gives a more in-depth look into the influence of foreign gas contents within the bubbles, such as contaminated gases, the thermal effects on bubble growth, convection due to relative motion between the bubble and the fluid, surface roughening effects, and non-spherical perturbations. However, Rayleigh Plesset equation used in this thesis assumes symmetry and the spherical shape of the bubbles. It ignores thermal effects and the presence of contaminated gases.

2.2.2 Schnerr-Sauer model

In bubble dynamics, during the growth and collapse of vapour bubbles, the resulting bubble collapse near the blade surface produces pressure pulses of magnitudes high enough to cause the subsequent collapse of more bubbles. After which, a global bubble collapse is initiated. The Schnerr-Sauer model provides a proper depiction of this pressure dynamics uninfluenced by the fluid viscosity (Schnerr and Sauer, 2001). It also ignores bubble growth acceleration. The homogeneous mixture approach defines the fluid as a mixture of water in its two phases. The model depicts the transition between these two phases. So, the mixture can be described with only a single set of equations.

The growth rate of bubbles is estimated as in equation 2.16 using the inertia growth model (Sauer, 2000).

$$v_r = \sqrt{\frac{2}{3} \left(\frac{p_s - p_\infty}{\rho_l} \right)} \quad (2.16)$$

Where, as earlier stated p_∞ is the pressure in the fluid domain and p_s is the saturation pressure.

The ratio of the volume of vapour in a cell and the volume of the full computational cell i.e. void fraction $\alpha = \frac{Vol_v}{Vol_v + Vol_l}$ is represented as:

$$\alpha = \frac{\frac{4}{3}\pi n R^3}{1 + \frac{4}{3}\pi n R^3} \quad (2.17)$$

The volume of vapour in a unit liquid would be taken to be: $\alpha_v = n \cdot \frac{4}{3}\pi R^3$. n is the number of bubbles in a unit volume.

From the equations above, the vapour production rate will then be calculated to be:

$$\frac{\partial \alpha}{\partial t} = (1 - \alpha) \left(\frac{4}{3}\pi R^3 + 1 \right)^{-1} \frac{d}{dt} \left(\frac{4}{3}\pi R^3 \right) \quad (2.18)$$

The second term depicts the change of vapour fraction per cell volume. The velocity field accrues divergence as a result of the bubble growth. Details can be found in Schnerr and Sauer, 2001.

2.2.3 Cavitation types

As the curl (rotation) of the velocity vector, vorticity measures the moment of momentum of a small spherical fluid by its centre of mass (Shapiro, 1961). Vortices are regions in a fluid body with a higher concentration of vorticity than other regions in the fluid. Cavitation is quite typical in these cores of irrotationality because of the low pressure in these regions. Cavitation is portrayed as the formation of vapour bubbles (or cavities) in the fluid in regions of low pressure. Figure 2.1 shows some common cavitation patterns.

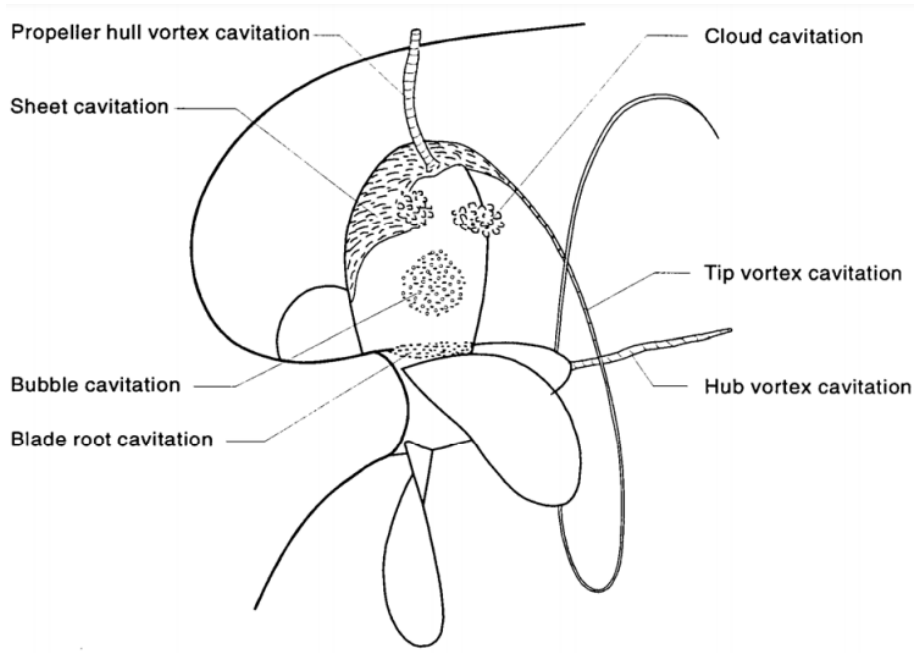


Figure 2.1: Common Cavitation Patterns on Ship Propellers ITTC, 2002

The propensity for cavitation to occur can be measured by the cavitation number i.e.

$$\sigma = \frac{p_\infty - p_v}{0.5\rho_l U_\infty^2} \quad (2.19)$$

Where, p_∞ is the static pressure at the point of focus in the domain.

2.2.3.1 Vortex cavitation

As earlier stated, in flows of high Reynolds number, regions of high vorticity are almost always present. Cavitation could start in the core of these vortices. For propellers and foil structures, the vortices are usually created at the tip of the blades.

The fluid traverses across the propeller blade from the high-pressure side to the low-pressure side results in vortex formation, which results in cavitation. They could incept from the leading edge of the blade planform or roll down the blade tip. When the latter happens, they are referred to as **Tip-vortex** (Shen et al., 2009).

Due to high azimuthal velocity and corresponding Reynolds number, the propeller rotations produce areas of high vorticity. In these irrotational cores are regions of low pressure. So, most often, cavitations could stem from these vortex cores. This is vortex cavitation.

According to (Bosschers, 2018), the transient oscillatory dynamics of a vortex cavity collision with fluctuations during blade passages results in reverberating production of broadband humps. Choi et al., 2009 examines the growth, oscillation, and collapse of bubbles grown due to vortex cavitation in cylindrical shapes in two and three dimensions.

2.2.3.2 Sheet Cavitation

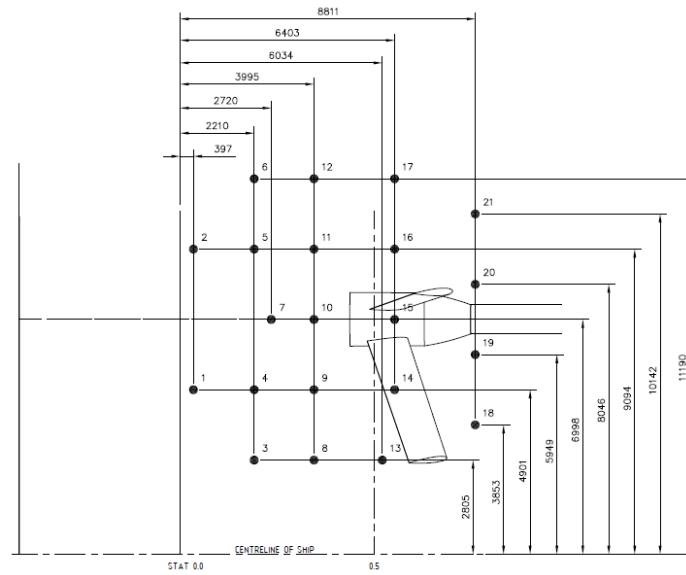
In specific scenarios, the mixture phase discontinuity forms a sheet on the blade's surface. This is due to minimum pressure on the blade surface. The cavity detachment is also initiated on the blade surface. Cloud cavitation could result due to re-entrant or side-entrant jet disrupting the formed sheet cavity.

These are depicted in figure 2.1 above.

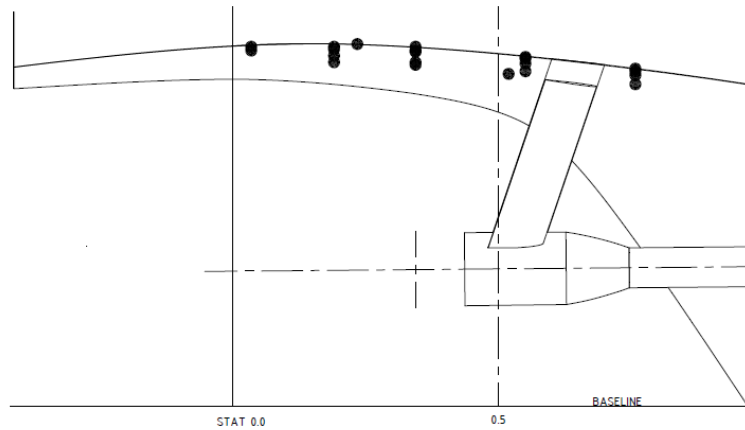
2.3 Hull-propeller pressure fluctuations

Hull pressure prediction experiments may be performed in Depressurized Wave Basins (DWB). In this, a model scale hull is utilized. Unfortunately, using the model scale results in discrepancies in the propeller wakefield prediction. In addition, due to scale effects and corresponding Reynolds number differences, the operating wakefield differs from full-scale to model scale. However, with CFD, these discrepancies are curbed if not eliminated (Van Wijngaarden, 2011).

In this thesis, twenty-one probes are placed at locations on the hull above the propeller. The pressure on these probes are reported and monitored. This corresponds to the experimental setup as seen in fig. 2.2.



(a) Top view



(b) Side view

Figure 2.2: Location of Pressure Transducers in both Experiment and CFD simulations

Cavitation inception is checked for in locations of low pressure. As earlier stated, it is checked in the cores of blade tip vortices for vortex cavitation. Therefore, the density and saturation pressure of the homogeneous liquid has to be defined appropriately at the experimental temperature ($17.3^{\circ}C$). The compressibility of the vapour contents, which usually fill the cavities, depends on the liquid's properties in the gaseous phase.

The cavitation number varies across the blade due to uneven hydrodynamic pressure. This is compared with the experimental results, and discrepancies could result from improper positioning of the probes in the CFD simulation.

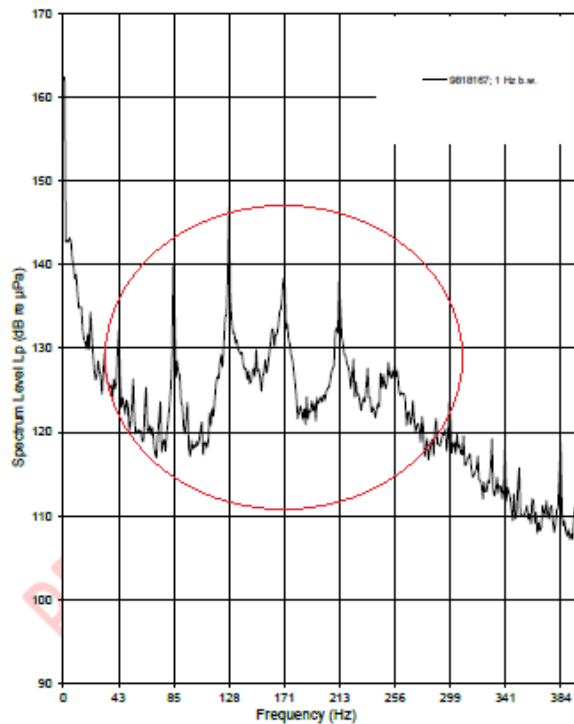


Figure 2.3: Sample of processed signal from a Cavitating propeller.

Figure 2.3 is a sample of a processed signal of a transducer over a cavitating propeller. It contains power spectral densities across a defined bandwidth (range of frequencies). It also shows impulses resulting due to resulting tip-vortex cavitation. These impulses are indicated in the red circled region.

2.3.1 Power Spectral Estimation

The pressure data accumulated from the model simulations is accumulated. This data will cumulate as deterministic signals. In order to validate the data, signal processing will have to be performed on it. In this case, a power spectrum estimation is performed.

The power spectral estimation is used to analyse and extract the frequency content of the data set. The primary focus of this is to get the spectral resolution and not the amplitude. The Spectral Amplitude estimator will aim to determine the Sound pressure levels. The Spectral Amplitude estimator is based on the conservation of energy (also called Parseval theorem) which states the total energy is conserved across both time and frequency domain as in equation 2.20 (Kelkar et al., 1983).

$$\int (s(t))^2 dt = \int (S(f))^2 df \quad (2.20)$$

The left-hand side represents the energy across the time domain; Correspondingly, the right-hand side represents the energy across the frequency domain per unit frequency, i.e. the Energy Spectral Density. Therefore, the Power Spectral Density (PSD) will be

$$PSD = \frac{RHS}{T} \quad (2.21)$$

Note: RHS is the right hand-side of equation 2.20. To obtain $S(f)$ in equation 2.20, we perform a Fast Fourier Transform (FFT) of the time domain data $s(f)$. This follows the lines of the Spectral Amplitude Estimator, which provides a periodogram using classical estimators based on FFT on spectrograms of data.

The Experimental data is given in spectral amplitudes. This is represented in Sound Pressure Levels against frequencies of data. The Sound pressure level assuming space-time invariant impedance for acoustic pressure as in this case will be taken as in equation (Urlick, 1983).

$$SPL = 20 \log_{10} \frac{p}{p_{ref}} \quad (2.22)$$

Where, p is pressure measure at an instance of time (the time difference between each datum of pressure, dt) and p_{ref} is the reference pressure level, taken as $1\mu Pa$ (Weissler, 1971).

2.4 Separation and Gamma ReTheta Transition model

2.4.1 Separation

At a certain point downstream along the surface of the bluff body, the main stream flow suddenly breaks away from this body of high Reynolds number. With the skin friction suddenly disappearing, the boundary layer thickness suddenly becomes zero downstream the flow. The point at which this happens is called the *Separation point* (**Brown1969**). This is the point at which the flow separates which could happen due to the upstream attached boundary layer encountering a sufficiently high pressure gradient.

2.4.2 $\gamma - Re_{\theta t}$ model

The $\gamma - Re_{\theta t}$ transition model is used to simulate the laminar to turbulent regions along the flow by modifying the transport equations for turbulence. It predict the outset of the laminar to turbulent transition along the bodies used in this thesis which are bodies of high Reynolds number in the turbulent boundary layer. The $\gamma - Re_{\theta t}$ transition model is a Correction based transition model devised by (Langtry and Blair, 2006) , specially for unstructured CFD codes. Like most other transition models, it uses a concept in which 0 depicts a fully laminar flow, and 1 depicts a fully turbulent flow. This is the concept of intermittency. The transport equation for intermittency is defined so that the evaluation of the vorticity based on Reynolds number is used. Thereby not requiring evaluation of momentum thickness Re , which will be used in a second

equation for the model definition. It relates quantities and characteristics of flow, such as the start of the transition to the pressure gradient, in two equations. The first equation is the intermittency transport equation as earlier stated. This evaluates kinetic energy production in the boundary layer leading from laminar to fully turbulent flow; The second is the Transition Momentum thickness Reynolds number transport equation. The first equation neglected this by using vorticity based on Reynolds number in equation 2.23 (Van Driest and Blumer, 1963). The second transport equation locates the transition onset,

$$Re_v = \frac{\rho y^2}{\mu} \frac{\partial u}{\partial y} = \frac{\rho y^2}{\mu}, \quad (2.23)$$

where, y is the distance from the wall and Ω the magnitude of the strain rate. The intermittency equation is as stated in equation 2.24

$$\frac{\partial(\rho\gamma)}{\partial(t)} + \frac{\partial\rho U_j \gamma}{\partial x_j} = P_\gamma - E_\gamma + \frac{\partial}{\partial x_j} \left[\left(\mu + \frac{\mu_t}{\sigma_f} \right) \frac{\partial\gamma}{\partial x_j} \right] \quad (2.24)$$

γ represents intermittency. P_γ is the production term and E_γ the destruction/relaminarization source term. These terms are defined in detail in Langtry and Blair, 2006. σ_f is a constant.

While, the transport equation for the transition momentum thickness Reynolds number is depicted as follows:

$$\frac{\partial(\rho \tilde{Re}_{\theta t})}{\partial t} + \frac{\partial(\rho U_j \tilde{Re}_{\theta t})}{\partial x_j} = P_{\theta t} + \frac{\partial}{\partial x_j} \left[\sigma_{\theta t} (\mu + \mu_t) \frac{\partial \tilde{Re}_{\theta t}}{\partial x_j} \right] \quad (2.25)$$

Where, $\tilde{Re}_{\theta t}$ is the momentum thickness Reynolds number. $\sigma_{\theta t}$ is a constant and the other terms are similarly defined as for the intermittency equation.

Using this method, as the vorticity Reynolds number increases. there is a corresponding increase in the shape factor (H). This is used to predict separation induced transition. i.e. $Re_v H$. Detailed literature on this can be found in Langtry and Blair, 2006, Langtry and Menter, 2005 and Menter et al., 2006.

2.5 STAR-CCM+

The commercial package Simcenter STAR-CCM+ is utilised for simulation. It is a multidisciplinary engineering package with an integrated user interface that provides detailed physics simulations. It is a CAE solution for solving both fluid and solid mechanics problems. The commercial package versions 15.02.007, 16.02.008 and 16.02.008-r8 are used in this thesis. The software utilises the SIMPLE algorithm to solve Navier-Stokes equations for both steady and unsteady flows. The PISO algorithm can also be used in place of the SIMPLE but only for unsteady flows.

Nonetheless, the SIMPLE algorithm is used for pressure-velocity coupling in

both steady and unsteady flows in this thesis. It offers different discretization methods to solve the discretised equations such as Upwinding schemes, central differencing, and Hybrid MUSCL 3rd-order/CD.

STAR-CCM+ provides varying cell shapes for both surface and volume meshing. From polygonal to prisms to generate structured or unstructured grids. The Gauss-Seidel point iterative method is used in this thesis. However, the commercial package also provides other methods such as Jacobi and Incomplete Lower-Upper (ILU).

2.6 Simulation Setup

2.6.1 Case Description

A ship model is provided. The hull has twin-screw high-skew fixed-pitch four-bladed propellers. The properties of the hull case are given in table 2.1 and the propeller in table 2.2.

Table 2.1: Ship Hull full-scale properties

	Hull		unit
	Design D	Ballast D	
Length between Perpendicular	225	225	m
Moulded Breadth on WL	32	32	m
Fore Draft	7	6.2	m
Aft Draft	7	5.4	m
Displacement	33722	27058	m^3
WSA bare hull	7958	7146.2	m^2
Block coefficient	0.669	0.648	
WPA coefficient	0.883	0.8	

Table 2.2: propeller properties

	Values	units
Diameter	5.8	m
Pitch ratio at 0.7R	1.22	
Prop Tip clearance	30%	
Blade number	4	
Rotation direction	starboard	

The approximate Reynolds numbers of bodies in the domain are 1.5×10^6 and 2.0×10^7 for the model propeller and model ship hull respectively.

Ship to Model Scale using Froude scaling is $\frac{1}{27.385}$.

The model ship design speed is 2.32m/s. Shaft speed of model propeller equates 640rpm. Therefore, the derived velocity of the model propeller at the rotation speed equates 10.7m/s.

2.6.2 Pre-processor

ITTC (ITTC, 2014) gives recommendations on computational domain dimensions. Figure 2.4 below shows the parent domain dimensions. The parent domain sums both the ship hull and the propeller rotating region domain.

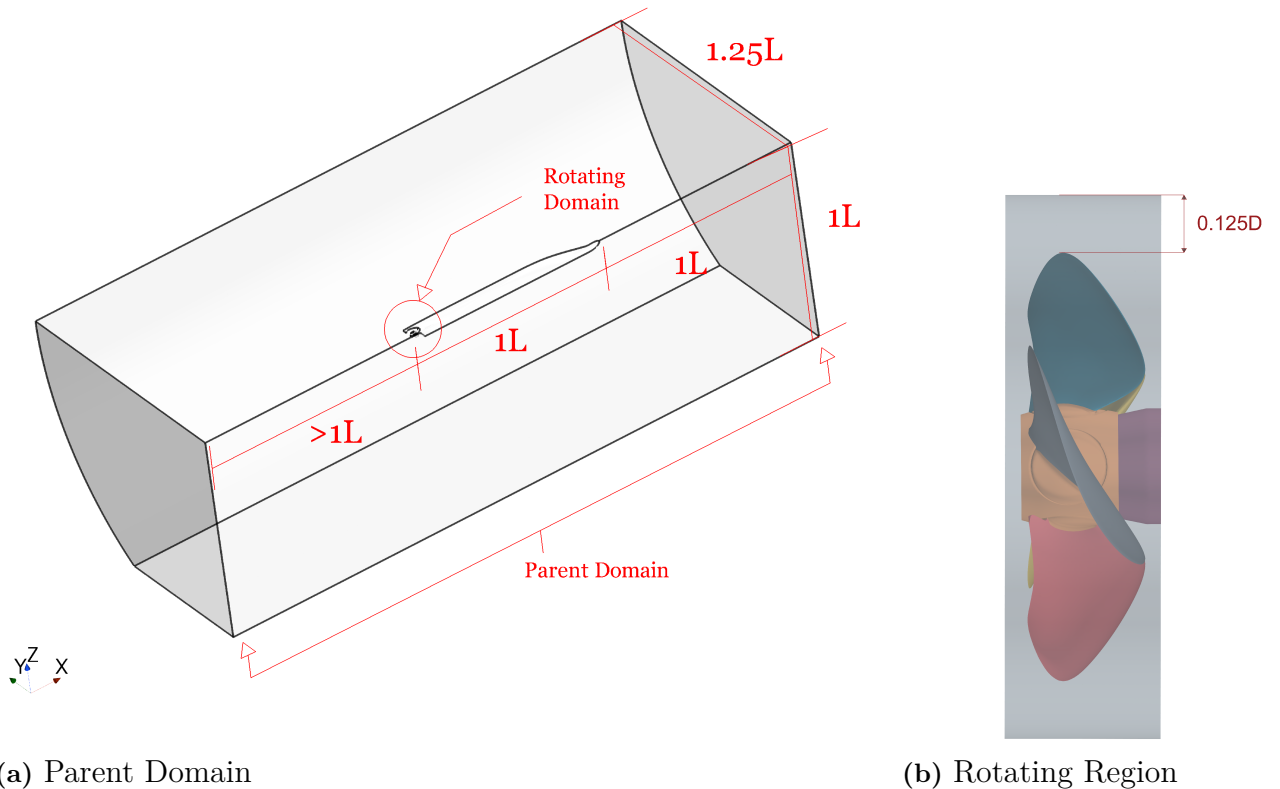


Figure 2.4: Domain

The rotating region is cylindrical. It has a diameter of $1.25D$. Figure 2.4 depicts this region. An internal interface lies between the two domain regions to transfer physical quantities.

The Menter SST - $k-\omega$ is used as briefly highlighted in section 2.1.1.1. The flow model is segregated and second order convection is used. The simulations are performed at a temperature of 20°C . Therefore, the saturation pressure and density of water are set accordingly.

2.6.3 Simulations Outline

Two sets of simulations are performed. One to capture the default conditions and propeller inflow wake, i.e. ensure matching thrust coefficient (KT), achieving convergence of the residuals. The other, the required post-processing data.

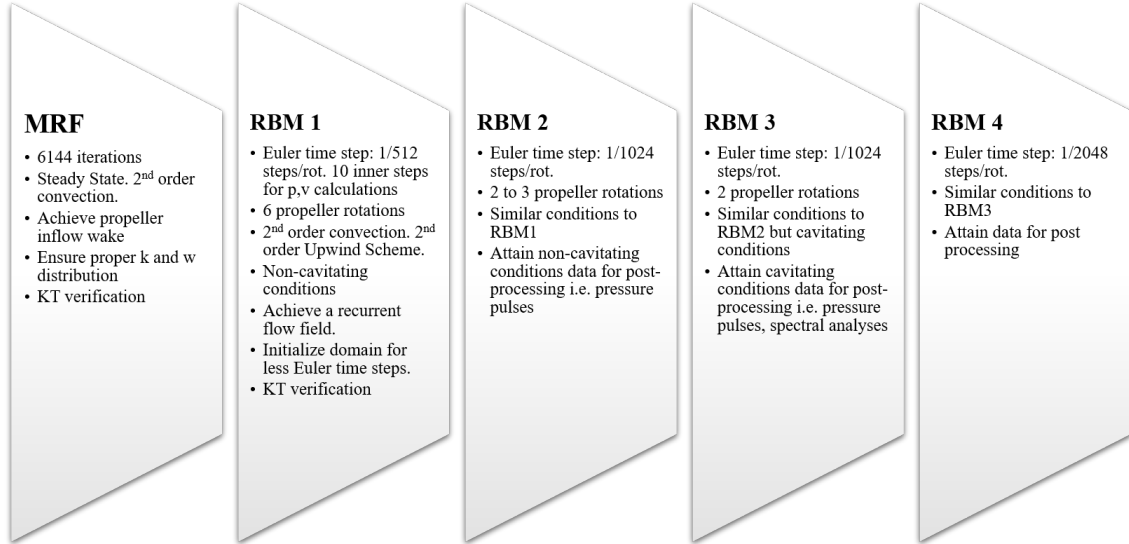


Figure 2.5: Simulations Outline

Firstly, a Moving Reference Frame (MRF) simulation is run for the former. This is a steady-state simulation that could span over 6000 iterations. Following, will be sets of Rigid Body Motion (RBM) simulations for the latter. The RBMs describe transient solutions in which the propeller rotates at pre-defined motion along its axis.

Four stages of RBM are run. The first details six propeller rotations in non-cavitating conditions. Using Euler time advancing, each time step consists of 512 steps. With ten inner iterations for pressure and velocity evaluation. The second order Upwind Scheme is used. This will be aimed to achieve a recurrent flow field, verification of the Thrust coefficient and initialize the domain for smaller Euler time steps. After which, the second set of RBM simulations will consist of two to three propeller rotations in non-cavitating conditions and smaller Euler time steps. It will consist of 1024 steps per rotation. The output data will serve for post processing consisting of data such as pressure pulses and cavitation number at non-cavitating conditions. The third stage of the RBM simulations will be a cavitating simulation, consisting of two propeller rotations. Post-processing data such as power spectrum densities will be attained for post-processing. The last and optional stage is same as the previous. However, Euler time steps of $\frac{1}{2048}$ will be used.

2.6.4 Mesh Setup

Most of the time spent in this thesis was used for grid generation—the breakdown of the pre-defined computation domain into cells to ensure proper discretization for numerical evaluation and implementation. The mesh is differentiated into two sects. The parent and rotating region. The parent mesh consist of the bare hull and also serves as a background for the propeller (rotating) region mesh. The parent region is useful for the hull-wake prediction and contains 67.3 million cells. While the rotating (propeller) region 17.3 million cells. Mesh refinements made are explained in sections 3.1.1 and 3.1.2. More refinements are made to ensure a proper transition from the parent domain to the rotating region; and proper capture of the ship to propeller wake. Parallel Polyhedral meshes are used for the rotating region to achieve a wall $y+$ distribution of 1 across the blade’s surface. In contrast, trimmer-cell meshes in the parent domain are implemented and aim for $y+$ values of less than one (<1) across the hull surface.

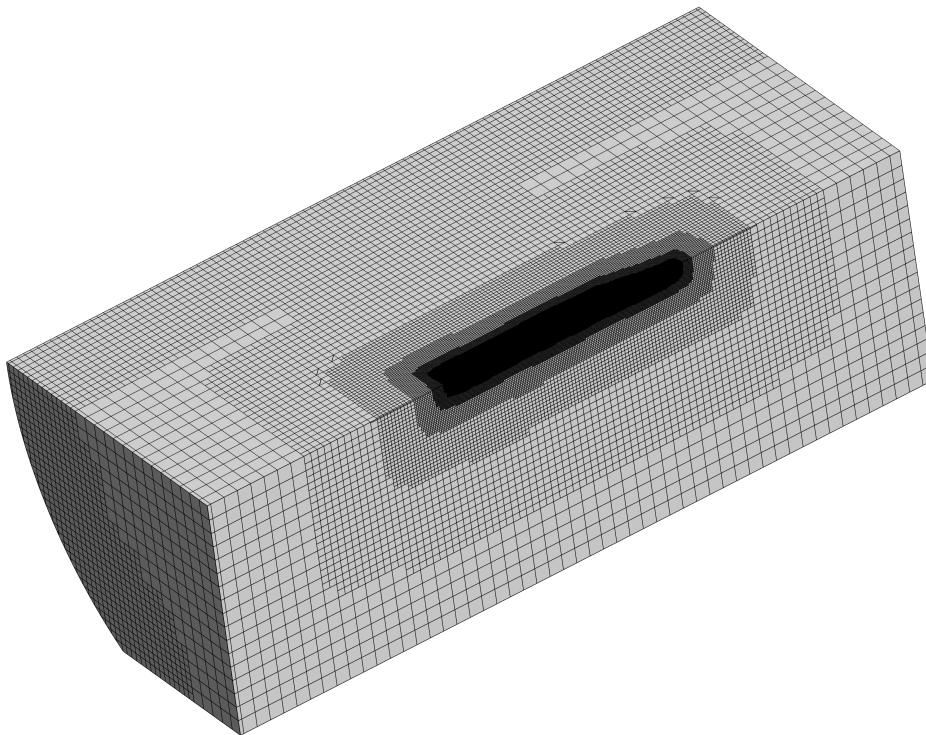


Figure 2.6: Mesh Overview

2.6.5 Solver details

The control volume method ensures the conservation of flow properties across the domain for each finite cell. An iterative approach is utilised to treat transport phenomena such as diffusion, convection and sustenance of source terms, i.e. associated with production and destruction of flow property. The SIMPLE algorithm is used to ensure proper coupling of primary pressure and

velocity terms. Gauss Siedel point iterative technique is used to apply this algorithm. This is implemented using the concept of Algebraic Multigrid. The commercial software STAR-CCM+ employs the Algebraic Multigrid acceleration concept to combat slow convergence. The Second-order upwind discretization method is used. Under-relaxation factors of 0.2, 0.8 and 0.8 are used for pressure, velocity and $K - \omega$ computations respectively.

3

Results

Using the methodology in chapter 2, simulations are performed. The ship to propeller wake, hull-pressure fluctuations and cavitation are captured. The hull-pressure data numerically derived is compared with experimental results.

3.1 Model case and CFD uncertainty analyses

3.1.1 Propeller Models

A high-skew propeller model in figure 3.1 is considered. The ship wake to the propeller is generated by analysing the velocity flow profile from the ship hull assigned to the propeller.

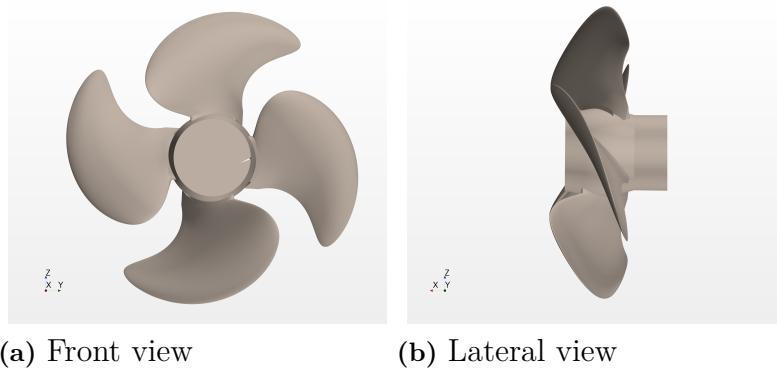
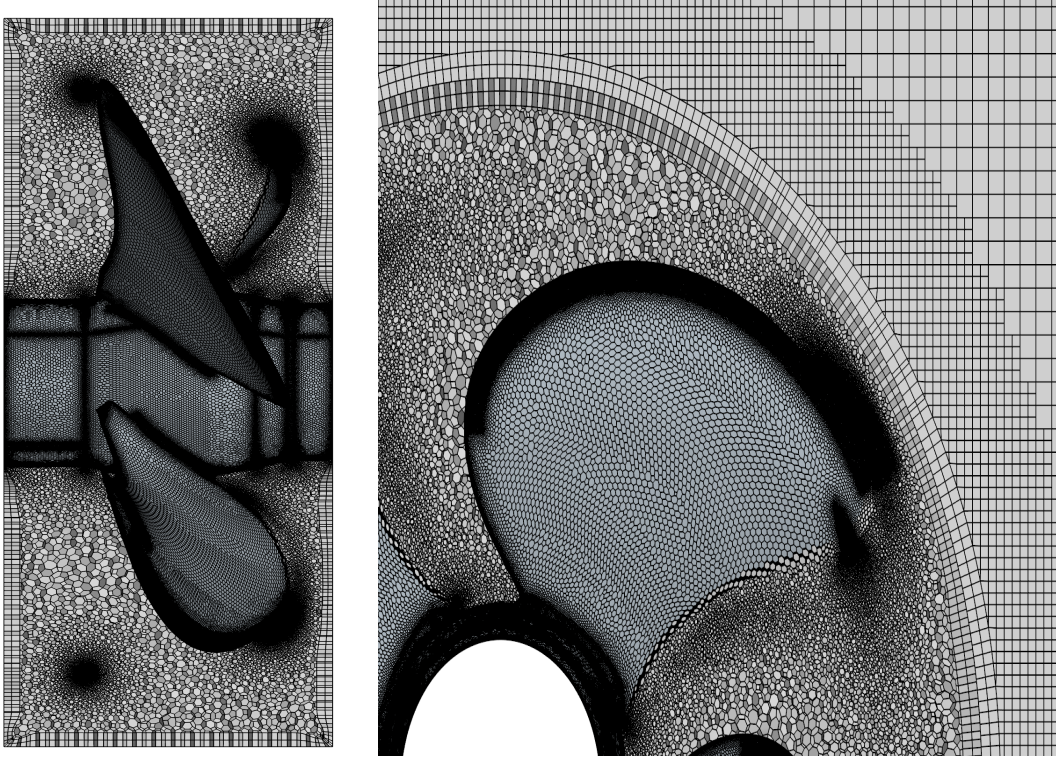


Figure 3.1: High skew propeller

Propeller-Induced Hull pressure experimental analyses have already been performed using this model. The test results were provided preceding this investigation. They consist of ship resistance test results, open-water tests results, service performance results and harmonic analyses, including hull pressure analyses.

The model is of similar characteristics with an almost equivalent propeller diameter. The propeller is right turning. Only the port-side propeller is depicted in the domain. The particulars of the propeller and assigned hull are stated in tables 2.2 and 2.1.

Figure 3.2a shows the propeller with the surrounding grid. Figure 3.2 shows the grid topology on a propeller blade. Figure 3.2b show the grid topology



(a) Propeller with surrounding grid (b) Figure showing mesh transition from rotating to background mesh

near-field the propeller blades. Figure 3.2b also shows the grids at the transition from a region of rotation at 1.25 the diameter of the propeller far field to the open-water test region in the computational domain. This region of rotation is defined by a cylindrical shape, whose diameter is 1.25 times the propeller diameter. The near-field propeller blade grid depicts a geometric progressive, smooth variation of the grid outward the blades' surfaces—this aids in capturing the viscous layer near the blade surface. The surface mesh around the interface of the near field rotating zone is characterised by high curvature, which grows span-wise both ways. At the interface of the rotating region are two different mesh setups. Outward the rotating zone is hexagonal shaped grids with minimal skewness.

In contrast, the region of rotation in itself utilises polyhedral cells. This is due to the complex geometries of the propeller. Each cell of the polyhedral mesh consists of a median of 14 faces.

Initially, the cell count for the propeller rotating region cumulates to 4 million cells. After, various fixes, which include cell skewness fixes, removal of non-positive cell volumes and cells causing turbulence kinetic energy (k) discrepancies. Refinements are added to occupy the position of the derived propeller vortex. This is obtained by extracting the vortices at a preset Q -criterion (Q) value (Hu et al., 2019). $Q \geq 50$ is used The cell count alleviates to 17.3 million cells. Figure 3.3 shows the cells in the near field vortices at $Q > 200$.

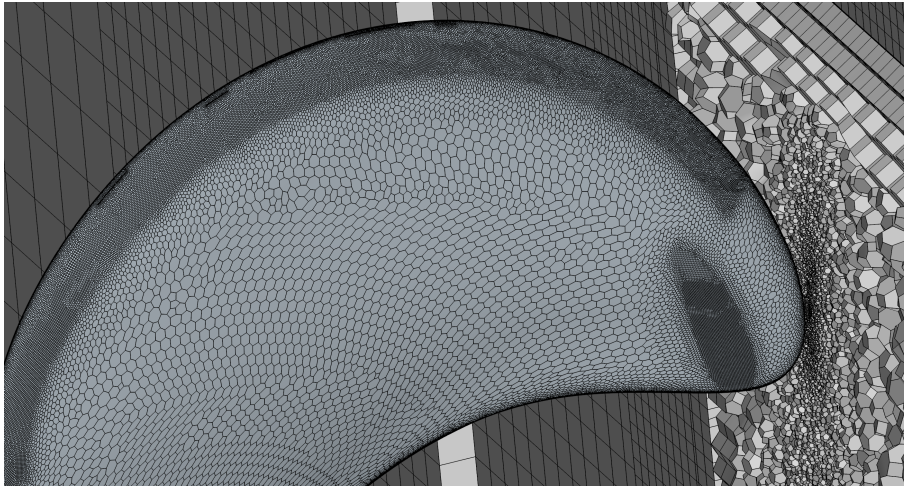


Figure 3.2: Propeller Blade Grid



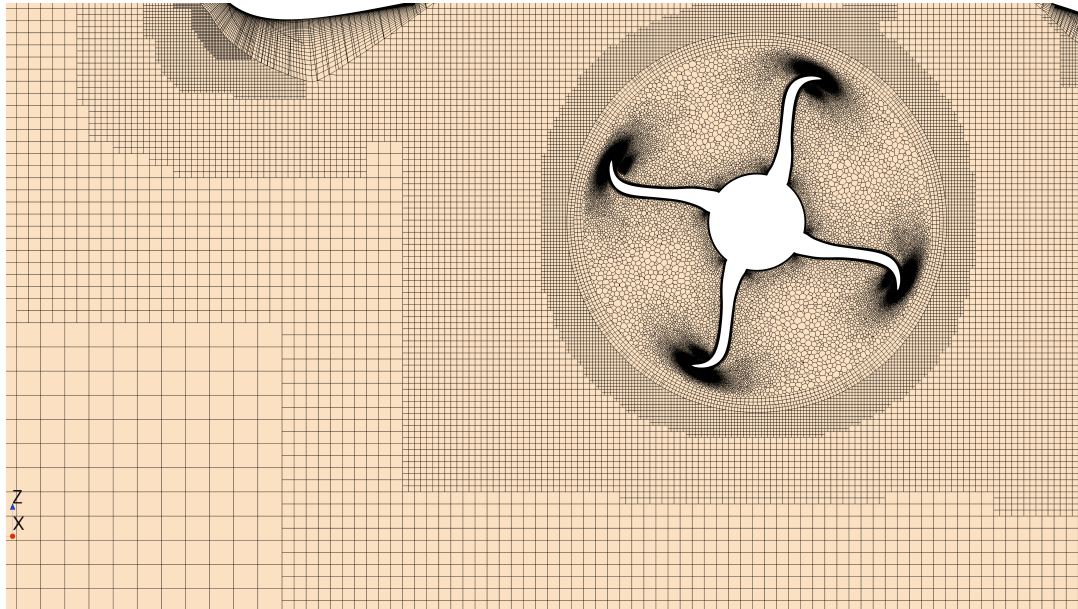
Figure 3.3: Cells near-field, $Q > 200$

3.1.2 Ship model

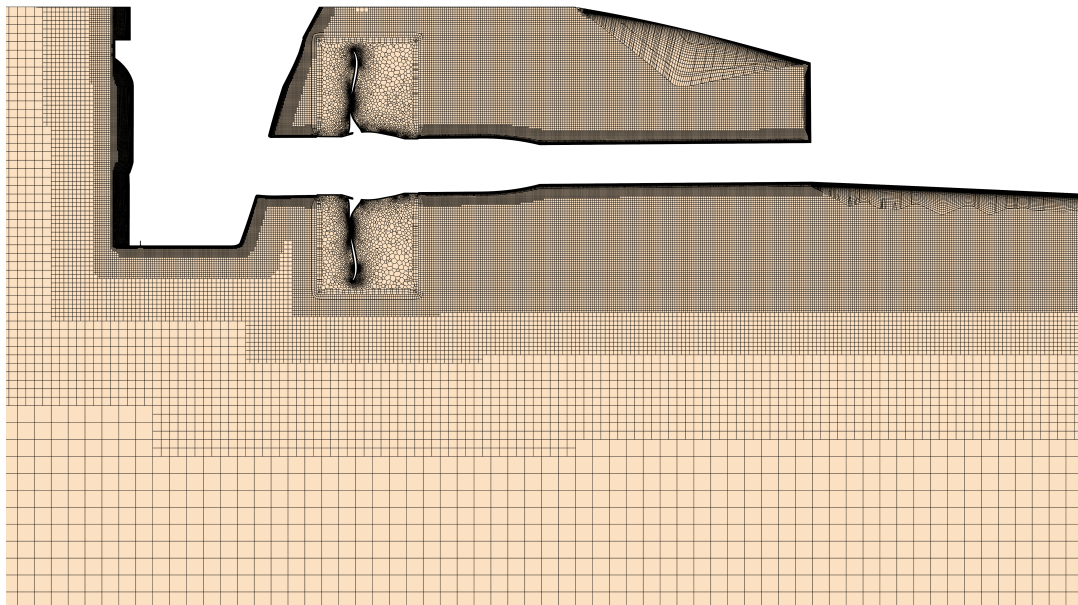
The flow profile provides the wake at which the propeller operates from the ship model, whose properties are described in table 2.1. The hull possesses a twin-screw propeller setup, which presents the starboard and portside of the ship from the longitudinal mid-ship section identical. Therefore, only the port side of the longitudinal mid-ship is considered.

The model scaled ship is placed in a modelled tank which serves as the background mesh for the propeller rotating grid region. Initially, the background mesh contains a cell count of 10 million, but this count is inflated after mesh fixes due to skewness, non-positive cells and high k valued cells are troubleshot. The resulting mesh consists of over 67.3 million cells. Figure 3.4b shows the resulting mesh. The wake from the ship to the propeller contains finer mesh to capture the propeller's flow profile upstream with high resolu-

tion.



(a)



(b)

The background mesh utilises hexahedral shaped cells trimmed at the input surface to achieve minimal cell skewness. These cells are aligned at the centre of the rotating propeller region. These cells are initially polyhedral but possess one or more edges or faces trimmed. This results in a lesser number of cells than a polyhedral cell-dominated region. Both propeller and ship surfaces have no-slip boundary conditions defined.

3.1.3 Solution Convergence and Thrust Coefficients

Checking the solution of the discretized equations with that of the continuous mathematical models for verification provided a rightly accurate result for the MRF simulations as in figure 3.4. As the simulation is switched transient, wiggles can be observed across the inner iterations discrediting the boundness of the solution. However, this could be a corollary of the use of the Upwinding scheme. The residuals are then elevated as there is a switch from non-cavitating to cavitating conditions.

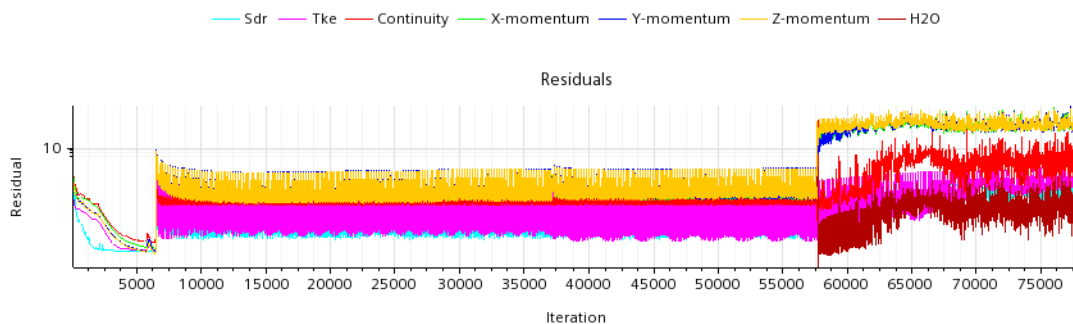


Figure 3.4: Residuals

The table below shows the disparities between the mean KT value and experimental value at various stages of the simulations.

Table 3.1: KT comparison (experimental value: 0.217)

	Values	deviation(%)
MRF	0.225	3.5
Non-Cav	0.2166	0.2

The torque coefficient (KQ) variates between 0.018 and 0.043. With a mean value of 0.0277 at an advance ratio, $J = 1.045$. The experimental value compared with KQ is that of a sister propeller and ship. The KT from open-water experiments at this advance ratio for the sister ship is 0.148. So, disparities are expected. A deviation of 22% is resultant from the mean value compared to the experimental value of the sister propeller which is 0.036.

Note that KQ, KT and J are coefficients which define the general characteristics of the propeller. Equations 3.1, 3.2 and 3.3 define these parameters.

$$KQ = \frac{Q}{\rho_l D^5 n^2} \quad (3.1)$$

$$KT = \frac{T}{\rho_l D^4 n^2} \quad (3.2)$$

$$J = \frac{V_A}{nD} \quad (3.3)$$

In equations 3.1, 3.2 and 3.3, Q represents propeller torque, T represents propeller thrust, VA represents the advance velocity, n represents the angular velocity of the propeller, and D represents the propeller diameter.

3.2 Wake Prediction

Figure 3.5 shows the ship wake at design draft and speed. It depicts the ship wake from midship portside at $0.975L_{pp}$. The propeller is a 4-bladed twin-screw fixed-pitch propeller. Unlike single-screw propellers, the wake of the twin-screw propeller is characterised by a jet structure which is viewed as a region of zero velocity in the figure. It is a vortex structure from the aft body of the hull. This structure impacts the blade, contributing significantly to the noise produced by twin-screw propellers ships. The nominal propeller upstream wake is predicted due to the MRF, which is a steady-state simulation. The wake depicts the contour distribution of velocity defined as $1 - \frac{V_x}{V_{inf}}$. V_{inf} represents the Inlet velocity.

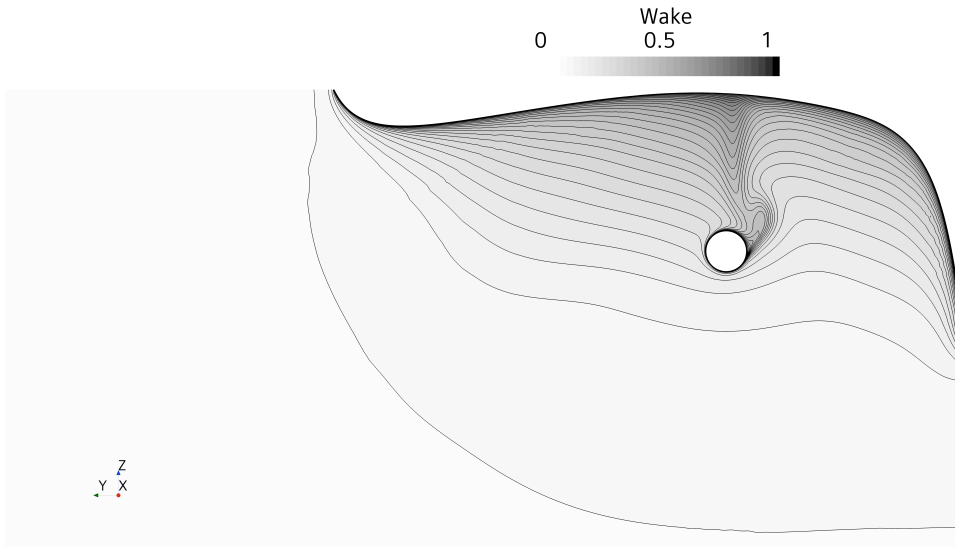


Figure 3.5: Ship to Propeller wake

3.3 Hull Pressure pulses

The plots in 3.6 focus on the spectral resolution of the pressure pulse levels at design speed. Alongside are the analytical and experimental data plots showing the Power Spectral Density at varying frequencies. However, the experimental data is of the sister case (hull and propeller). Therefore, discrepancies are expected. Figure 3.6 depicts the pressure levels on *probe 5* of the 21 probes as defined in fig. 2.2.

3.3.1 Data Comparison

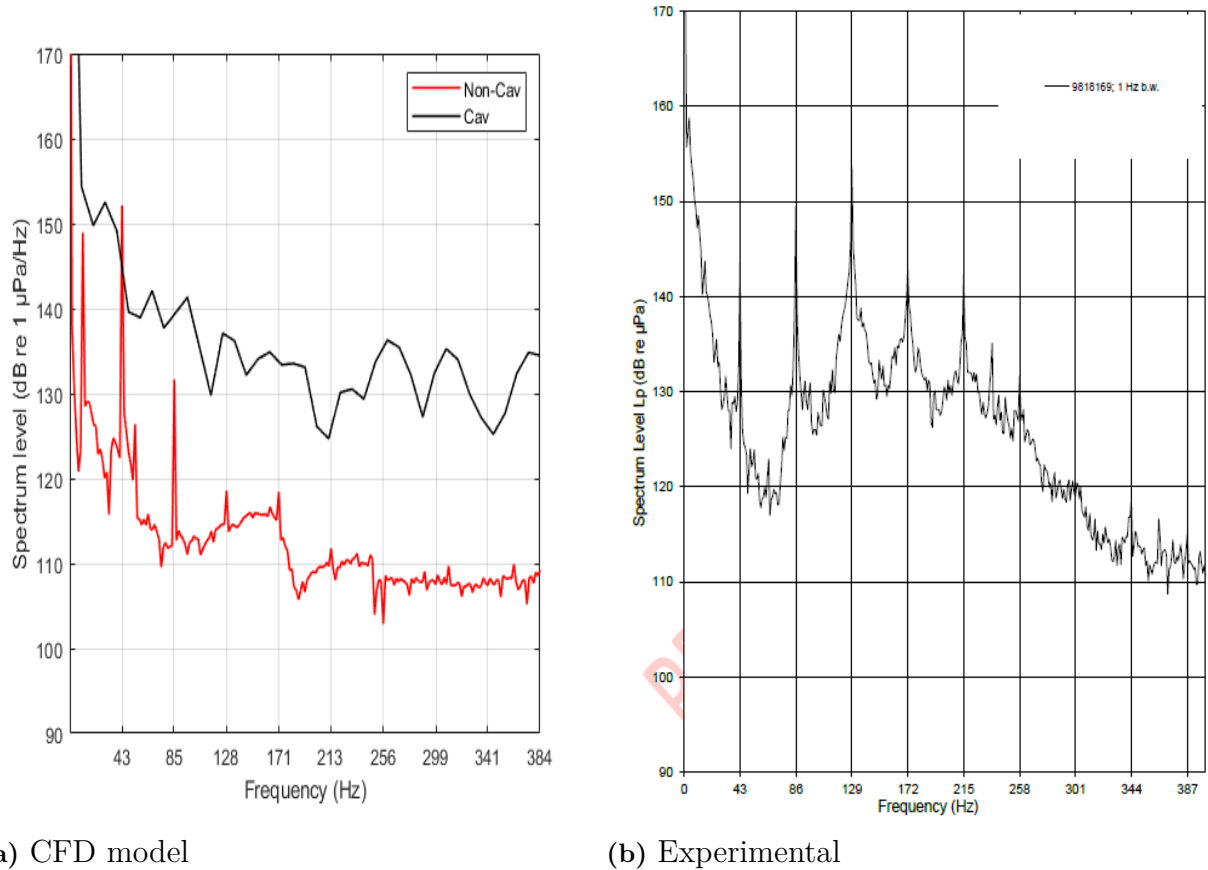


Figure 3.6: Spectral Analyses Comparison

Figure 3.6 shows the spectral distribution of the pressure pulses in power spectral density per frequency ($1Hz$). Spikes across the broadband characterise the spectrum of the pressure on the hull at BPFs. With a derived model propeller speed of 10.67rpm, the BPFs are at 42.68Hz. These can be seen as impulses across the narrow-band spectrum which can be accredited to the occurrence of cavitation at those frequencies, both consisting of tip-vortex and detached sheet-tip cavitation. Acoustically, this will be heard as "popping bubbles" in copious numbers. In reality, these are imploding bubbles of vapour, as explained in 2.2. The more significant spikes at narrow-band at the inception are accredited to cavitation and possible pressure suction as the blade passes under the hull. Occasionally, more spikes are recurrent, but a slow logarithmic decay can also be identified in the non-cavitating solution. Spectral flatness can be seen across the spectrum in the cavitating simulation (see fig. 3.10). The number of frequencies measured for the cavitating and non-cavitating solutions are 4102 Hz and 1856 Hz respectively. This highest SPL captured are at 9.6Hz and 42.7Hz for cavitating and non-cavitating conditions respectively. This might be due to inclusion of sheet cavitation in the

cavitating solution.

The PSD plots for the CFD model for cavitating conditions (figure 3.7) does not identify some expected distinct tonal components of the data. It is characterised by a high amount of Spectral flatness. The spikes in the data are spatially distributed and details are neglected if compared to the experimental data plots. The frequencies of the tonals are also a bit off BPF. And achieved spectrum level of CFD model are sometimes higher than that of the experimental.

However, for non-cavitating conditions as in figure 3.9, unlike in cavitating conditions, frequency resolution of the PSDs are much finer. Therefore, distinct tonals are more often identified. The tonals are also identified at BPF. Difference in amplitude exists but these discrepancies are expected as the data for comparison is that of a sister case.

3.3.1.1 Analyses of Variance

Analysis of Variance (ANOVA) is list of statistical methods to analyse differences among mean values. Firstly, the Spectral densities are broken down into different frequency bands. After which, the PSDs are averaged for each band. Then, an ANOVA is run. Table 3.3 shows the output data from the Variance Analyses. On the tables, SS represents the sum of squares of the variances, df represents the degree of freedom associated with each row in the table. This is the number of bands created minus one. MS is the Mean squares for each table row, which is the ratio $\frac{SS}{df}$. F is the ratio of the MS of the data compared.

Table 3.2: Analyses of Variance of Sound Pressure Levels for cavitating conditions

row		SS	df	MS	F
1.	CFD model data and exp.	8077.0	42	192.31	2.20
	Error in CFD model data and exp.	3663.6	42	87.23	
2.	CFD model data and exp. (sister case)	8916.3	42	212.3	5.82
	Error in CFD model data and exp. (sister case)	1532.4	42	36.5	
3.	Both exp. cases	6008.92	42	142.07	5.42
	Error in both exp. cases	1108.28	42	26.388	

Table 3.3: Analyses of Variance of Sound Pressure Levels for non-cavitating conditions (CFD model against Experimental for sister case)

	SS	df	MS	F
CFD model data and exp.(sister case)	38511	225	171.16	4.19
Error	9190.5	225	40.85	

To analyse the data in table 3.3, we review what an analyses of data between two indifferent data will look like in table 3.4.

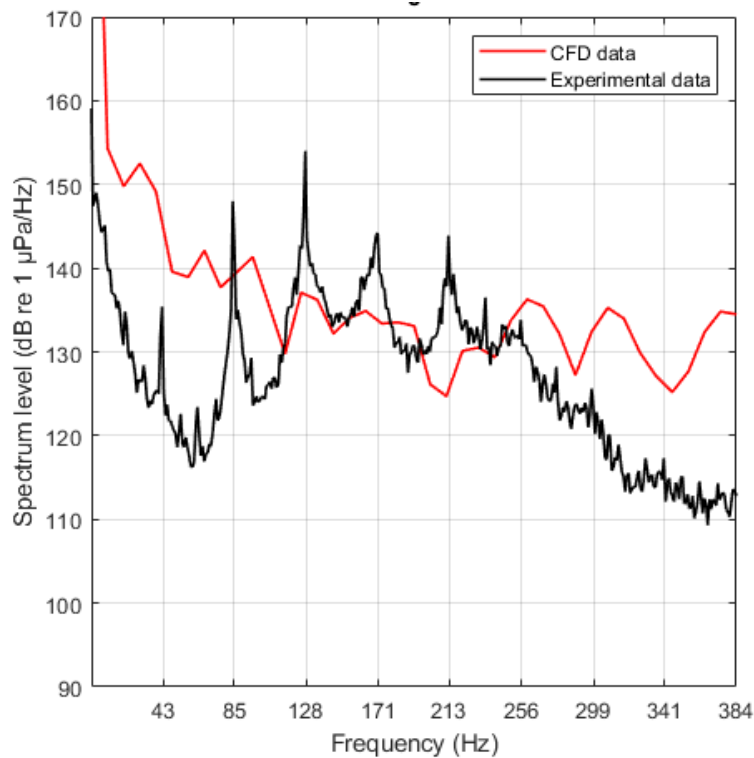


Figure 3.7: Spectral Analyses Comparison for Cavitating condition between CFD model and Experimental

Table 3.4: Sample ANOVA for two data with same SPL

	SS	df	MS	F
Error	3625.03	42	86.31	0
	0	0	∞	

In table 3.4, The ratio of the mean squares (MS) for each frequency sums 86.3. The second row "Error" stands for the variability of the data unaccounted for. Therefore, it depicts the default error expected between the data. A df of zero as in the sample ANOVA shows zero degree of freedom i.e. zero pairs of data frequencies with varying data. And, an SS of zero represents the sum of the square of the variance, which is zero as expected. The MS is ∞ because of zero degrees of freedom (number of pairs of data with variability).

Back to the analyses of variance of the CFD model data. The expected discrepancies between the data from the CFD model analyses and the experimental data are the values in row 3 of table 3.3. However, the rows 1 and 2 show the resultant discrepancies.

The spectral flatness of the signals (cavitating and non-cavitating) are 0.9973 and 0.9970 respectively. Spectral flatness is ratio of the geometric mean of the Fourier Transform (FT) of a signal to its arithmetic mean (Boashash, 2015). A spectral flatness of 1 sounds similar to white noise. The seemingly flatness for cavitating condition could be due numerical or post-processing errors.

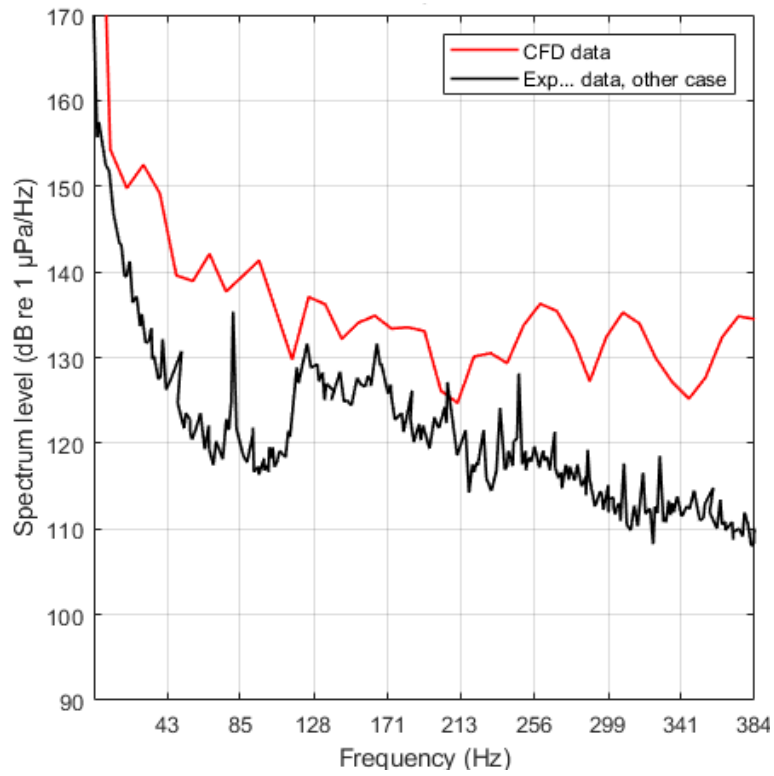


Figure 3.8: Spectral Analyses Comparison for Cavitating condition between CFD model and Experimental (Sister case)

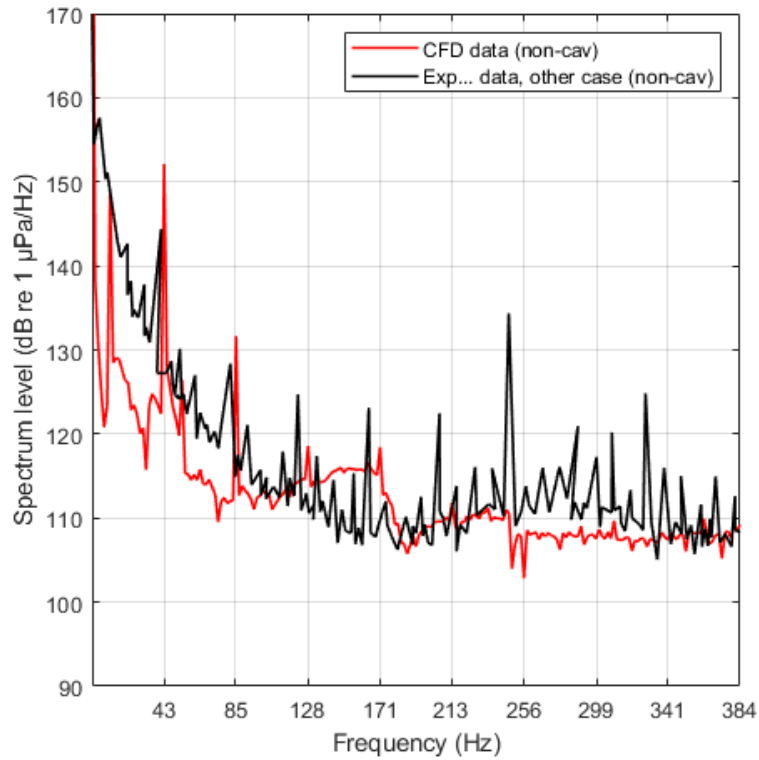


Figure 3.9: Spectral Analyses Comparison for Non-cavitating condition between CFD model and Experimental (Sister case)

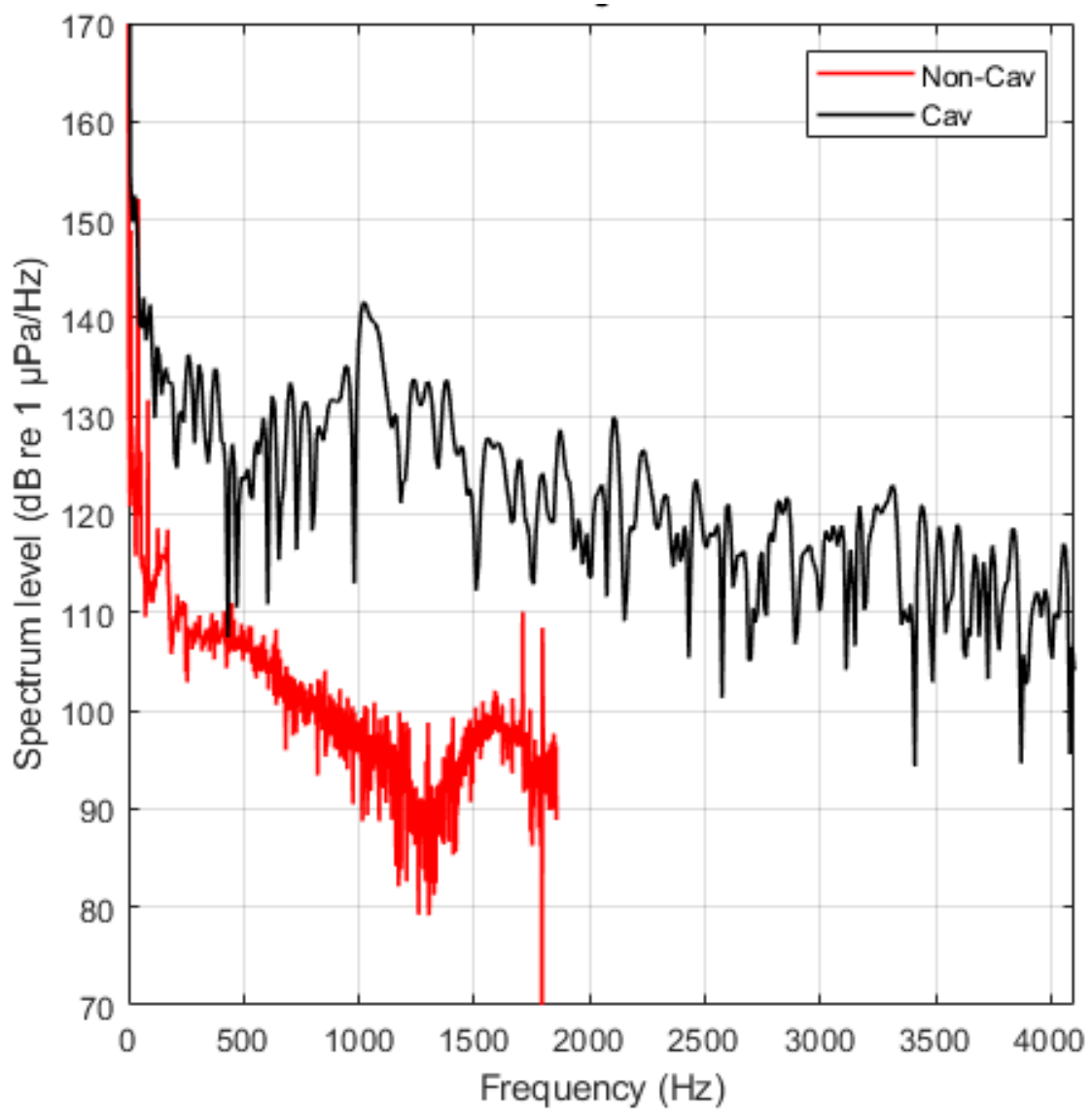


Figure 3.10: Full Spectral Analysis of Probe 1 data

3.4 Cavitating Pattern

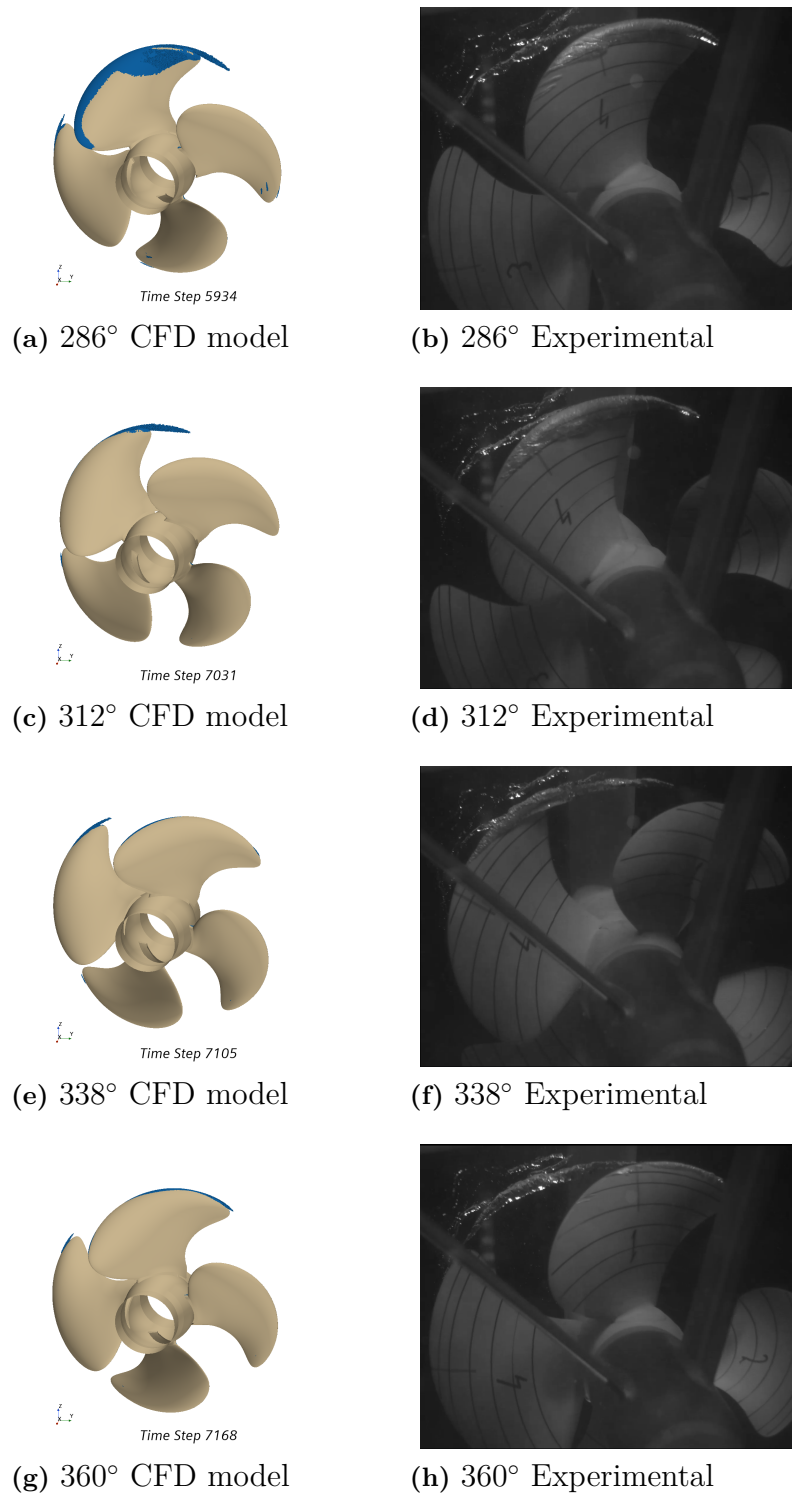
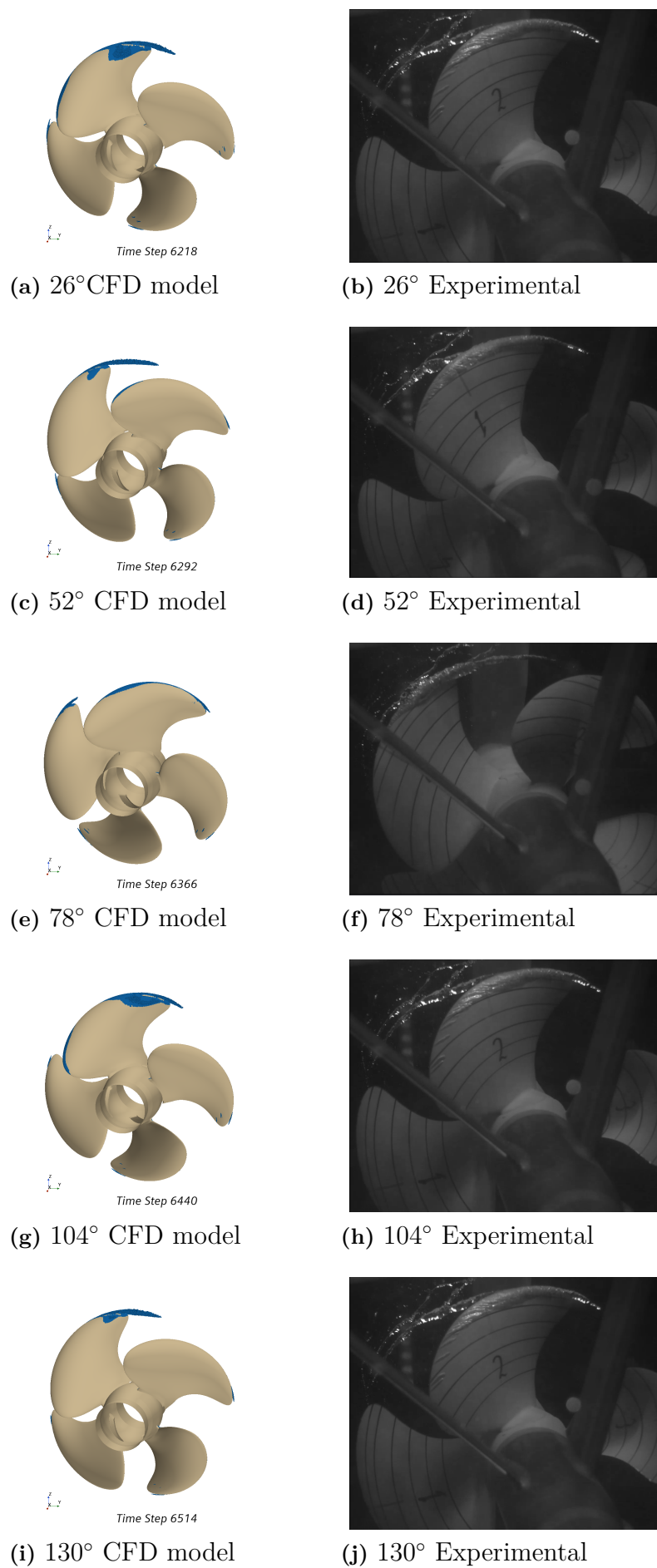


Figure 3.13: Cavitation comparison

**Figure 3.11:** Cavitation comparison

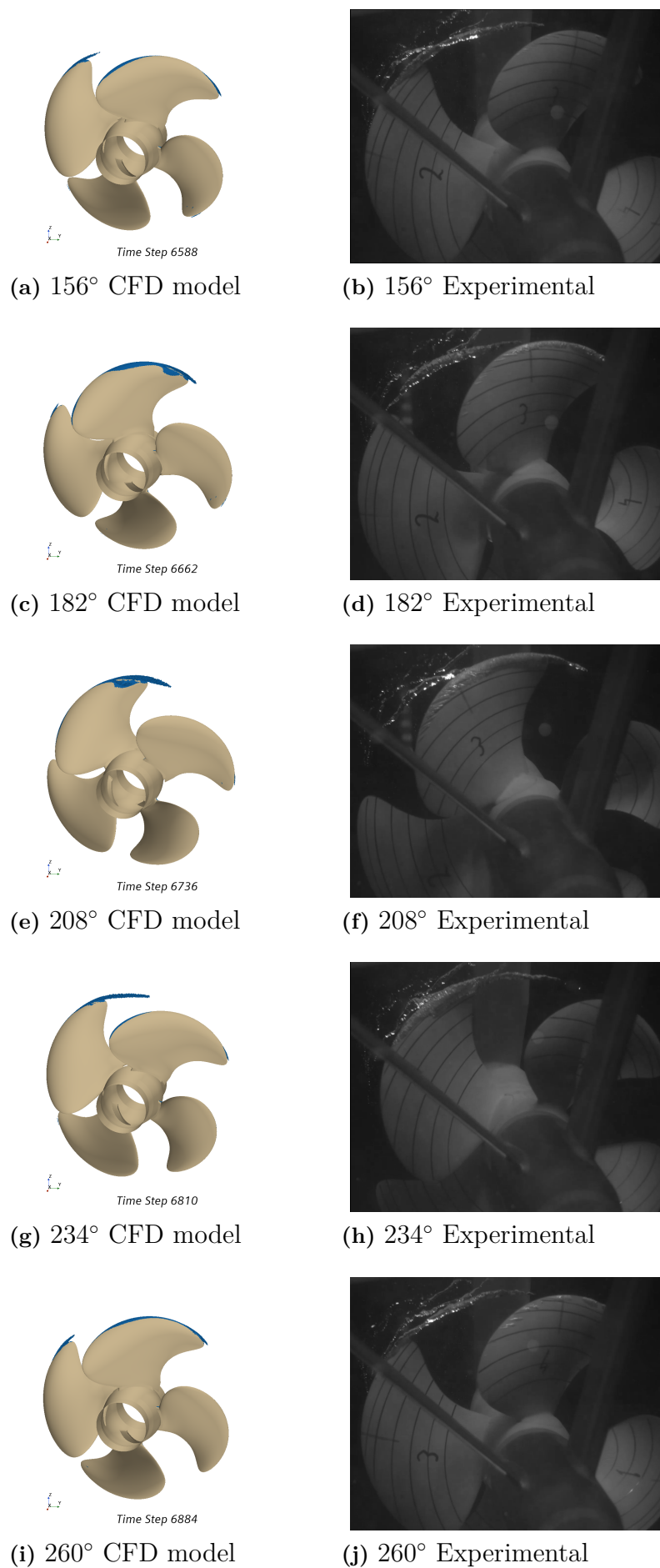


Figure 3.12: Cavitation comparison

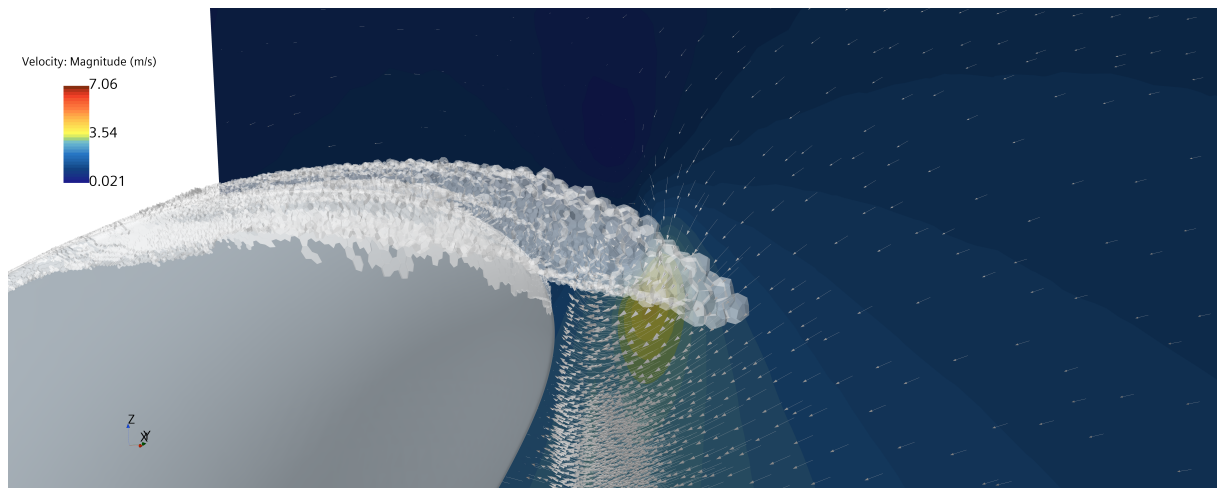


Figure 3.14: Irrotationality at center of cavity

Figures 3.11, 3.11 and 3.13 show the resultant cavities at different angles of rotation for both experimental and CFD model setups. These show astute similarity.

Cavities are formed initiated at each blade passing. There are resultant cavities formed at the tip of the propeller blade upon impact (i.e. 26°). This is then detached from the tip in a vortex (i.e. 52°). This is a sample of the resultant detached tip-vortex cavitation. At 78° , the remaining cavities from earlier make impact with the leading edge of the following blade. This results in short-lived leading wedge vortex cavities. It is shortly detached into the tip-vortex cavities. The vapour structure on the blade at 26° are characterised sheet and some cloud cavities. A resultant vortex cavity is attached to the sheet cavities at the blade tip, i.e. Attached sheet-tip cavities. These attached sheet-tip vortex cavities initially increase in radius downstream due to vortex strengthening as vorticity rolls up. The increase in radius of the vortex cavities structure is followed by a decrease as the core of the irrotational structure increases in radius downstream, as seen at 52° . The pressure in the centre of this irrotational vorticity structure can be attributed to the circular distribution of the velocity azimuthally as in figure 3.14.

The structure at 78° consists of cavities from the preceding blade passage. What can be identified as a sheet which initiates from the leading edge down the blade tip. This is probably resultant due to the skewness of the blade, which then leads to a closure as seen at 104° which might be a closure-vortex. The cavities structure is characterised by a sheet and does not increase in radius downstream. This is because the cavities do not possess so much strength to retain the size of the cavities. Another sample of this can be seen on the blade at 286° . While that of the attached sheet tip-vortex cavitation can be seen at 234° .

4

Conclusion and Discussions

4.1 Validation and Verification of Methodology

A twin-screw vessel with two four-bladed propellers is being analysed. Hull pressure data and resulting cavitation are being examined. Initially, experimental data is provided for these propellers. These data are then validated against data from a CFD model scale prediction. The CFD model scale predicted data are the results of an investigation using RANS.

One query is about the amplitudes of the power spectral densities for the CFD model prediction. Compared to that of the experiment, the difference is obvious. Disparities are expected. To check these disparities, the variance analyses for the cavitating conditions in table 3.3 can be used. The expected mean square of the variance (MS) is 142 while the achieved MS for the CFD model against the experimental for the sister case is 212. This shows a high per cent discrepancy. The residual error expected is 26.388. However, the achieved residual error is 36.5. Which shows less disparities resulting from the error. Even though data between both experimental cases (main and sister cases) for the non-cavitating conditions are not available for evaluation, comparing the CFD model in non-cavitating case to the Experimental sister case, the resulting mean error is less (171.2) with a mean square ratio of 4.2. With this, it is obvious that there are less discrepancies from residual errors and much more from the numerical prediction for the data of the cavitating simulations. This could attributed to the lack of a good mesh for numerical prediction in cavitating conditions. For non-cavitating conditions, a coarse mesh properly spatially distributed would provide acceptable predictions with an accurate wake prediction. Another possibility is post processing errors, as experimental data was not accurately extracted. However, if discretization errors are fixed, the RANS method does produce a near accurate prediction of the pressure pulses at first order blade passing frequencies (BPF). The transition between the background (core) mesh and the rotating region could also affect the wake prediction. Therefore, a proper transition ratio between the propeller rotating region and the background mesh is aimed at. This is done by ensuring equal sizes and distribution of cells at the transition layer for both background and rotating region.

4.1.1 Frequency Resolution

Imperative in Fast Fourier Transform of data in time series to frequency domain is frequency resolution. A properly resolved signal will be fine enough to identify tonal components autonomous of noise. To improve frequency resolution, the sampling frequency could be decreased or the number of samples could be increased. Thereby, increasing frequency bins. Frequency bins are the differences between frequency samples in a frequency domain data. They are intervals between data samples.

Reducing the sampling frequency is illogical as it would decrease the frequency range. So, the next option is to increase the number of samples. In this investigation, to do that will be to perform more simulations which were not affordable. Also, the commercial software normalises extracted data to export a maximum of 5000 samples. This limits the amount of samples available for analyses. Even though, smaller time steps are used corresponding to Euler time steps as low as $9.15 * 10^{-5}$ seconds per time-step. The resulting sampling intervals are $1.22 * 10^{-4}$ and $2.69 * 10^{-4}$ for cavitating and non cavitating conditions respectively. Therefore, improving the spectral resolution was not performed which affected the data utilised, and correspondingly, the results of the spectral analyses.

As a consequence of these, the frequency resolution is not fine enough to pinpoint much specific tonal components of the frequency domain data.

4.2 Cavitation and Hull-Pressure Fluctuations

As the propeller rotates in the ship wake, the resulting pressure fluctuations can be observed to occur during the blade passage under the hull surface. This possibly results in pressure suction causing the occasional pressure pulses detected by the transducers. Cavitation can be seen in various forms such as closure vortex, sheet, and tip vortex.

5

Future Work

A mesh independence studies was not performed. Therefore, the accuracy of the solution could have been affected by this. Future engagements should include data from varying mesh. The limitation to this is the requirement for accuracy at different project stages. The propensity of the dependence of the solution to the mesh is higher at the start of the MRF and switch to cavitating conditions. Therefore, occasional mesh fixes to achieve an independent solution has to be made at different points in the simulation. This repetitive step consumes computational resources and time. However, a successful independent solution will provide much more accurate results.

The influence of the other underwater appendages such as brackets and rudders should be investigated. The velocity profile on the impact on the blade varies from that of the ship at $0.975L_{pp}$ aft bow. The impact of the jet from the region of irrotationality in the ship wake on the blade could be a good case for investigations.

The free surface wake was also neglected in this project. Therefore, the results are not accurately a match compared to real-life scenarios. In addition, the inclusion of the free-surface wake could be burdensome to the numerical solution. However, if this is successfully implemented, the accuracy of the result in comparison to reality would be significantly improved. The information about the inclusion of the free surface in the model experiment is not known.

.

Bibliography

- Boashash, B. (2015). *Time-frequency signal analysis and processing: A comprehensive reference*. Academic press.
- Bosschers, J. (2018). Propeller tip-vortex cavitation and its broadband noise.
- Brennen, C. E. (2014). *Cavitation and bubble dynamics*. Cambridge University Press.
- Choi, J., Hsiao, C.-T., Chahine, G., & Ceccio, S. (2009). Growth, oscillation and collapse of vortex cavitation bubbles. *Journal of Fluid Mechanics*, 624, 255–279.
- Davidson, L. et al. (2020). Fluid mechanics, turbulent flow and turbulence modeling. *Chalmers University of Technology, Goteborg, Sweden (August 2020)*.
- Ekh, M. (2017). Mechanics of solids & fluids—introduction to continuum mechanics. *Report, Div. of Material and Computational Mechanics, Dept. of Applied Mechanics, Chalmers University of Technology, Göteborg, Sweden*.
- Erbe, C. (2011). Underwater acoustics: Noise and the effects on marine mammals. *A Pocket Handbook*, 164, 9–10.
- Guo, C.-y., Xu, P., Wang, C., & Kan, Z. (2019). Numerical and experimental study of blockage effect correction method in towing tank. *China Ocean Engineering*, 33(5), 522–536.
- Hu, J., Zhang, W., Sun, S., & Guo, C. (2019). Numerical simulation of vortex–rudder interactions behind the propeller. *Ocean engineering*, 190, 106446.
- ITTC. (2002). Testing and extrapolation methods. propulsion; cavitation. description of cavitation appearances. 75-02-03-032. *ITTC Recommended Procedures and Guidelines*.
- ITTC. (2014). Practical guidelines for rans calculation of nominal wake. *ITTC Recommended Procedures and Guidelines*.
- Kelkar, S., Grigsby, L., & Langsner, J. (1983). An extension of parseval’s theorem and its use in calculating transient energy in the frequency domain. *IEEE Transactions on Industrial Electronics*, (1), 42–45.
- Kozaczka, E., & Grelowska, G. (2004). Shipping noise. *Archives of Acoustics*, 29(2).
- Langtry, & Blair, R. (2006). A correlation-based transition model using local variables for unstructured parallelized cfd codes.
- Langtry, & Menter, F. (2005). Transition modeling for general cfd applications in aeronautics. *43rd AIAA aerospace sciences meeting and exhibit*, 522.
- Menter. (1992). Improved two-equation k-omega turbulence models for aerodynamic flows. *Nasa Sti/recon Technical Report N*, 93, 22809.
- Menter, Langtry, R. B., Likki, S., Suzen, Y., Huang, P., & Völker, S. (2006). A correlation-based transition model using local variables—part i: Model formulation.

-
- Rayleigh, L. (1917). Viii. on the pressure developed in a liquid during the collapse of a spherical cavity. *The London, Edinburgh, and Dublin Philosophical Magazine and Journal of Science*, 34(200), 94–98.
- Rijkema, D., Starke, B., & Bosschers, J. (2013). Numerical simulation of propeller-hull interaction and determination of the effective wake field using a hybrid rans-bem approach. *3rd International Symposium on Marine Propulsors*, (May), 421–429.
- Ross, D. (1976). Mechanics of underwater noise., 252–254.
- Sauer, J. (2000). Instationär kavitierende strömungen-ein neues modell, basierend auf front capturing (vof) und blasendynamik. *Diss., Uni Karlsruhe*.
- Schnerr, G. H., & Sauer, J. (2001). Physical and numerical modeling of unsteady cavitation dynamics. *Fourth international conference on multiphase flow*, 1.
- Shapiro, A. H. (1961). *Vorticity*. Massachusetts institute of Technology.
- Shen, Y. T., Gowing, S., & Jessup, S. (2009). Tip vortex cavitation inception scaling for high reynolds number applications. *Journal of Fluids Engineering*, 131(7).
- Stern, F., Kim, H., Patel, V., & Chen, H. (1988). A viscous-flow approach to the computation of propeller-hull interaction. *Journal of Ship Research*, 32(04), 246–262.
- Urick, R. J. (1983). Principles of underwater sound, mcgraw-hill. *New York*.
- Van Driest, E., & Blumer, C. (1963). Boundary layer transition-freestream turbulence and pressure gradient effects. *AIAA journal*, 1(6), 1303–1306.
- Van Wijngaarden, H. C. J. (2011). Prediction of propeller-induced hull-pressure fluctuations.
- Versteeg, H. K., & Malalasekera, W. (2007). *An introduction to computational fluid dynamics: The finite volume method*. Pearson education.
- Weissler, P. G. (1971). Ansi-1969 standard reference threshold sound-pressure levels for audiometers: Some comments. *The Journal of the Acoustical Society of America*, 49(4B), 1319–1320.

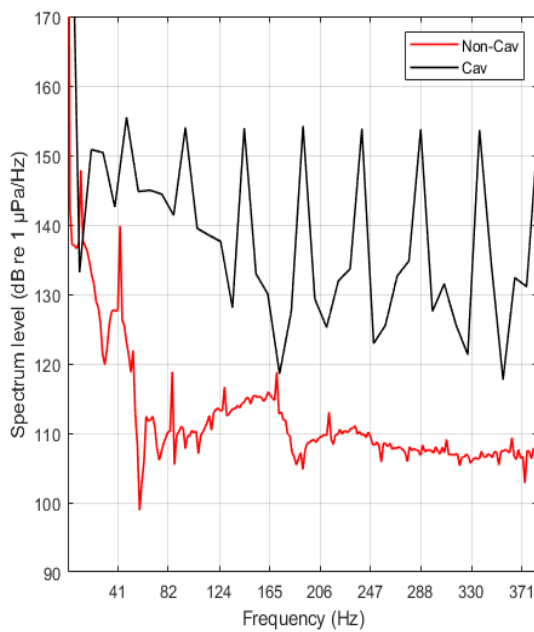
A

Appendix 1

Below are Spectral Analyses of the Hull-pressure data across the 21 probes.

Figure A.1: Spectral Analyses Comparison, Probe 2

(a) CFD model scale predicted



(b) Experimental

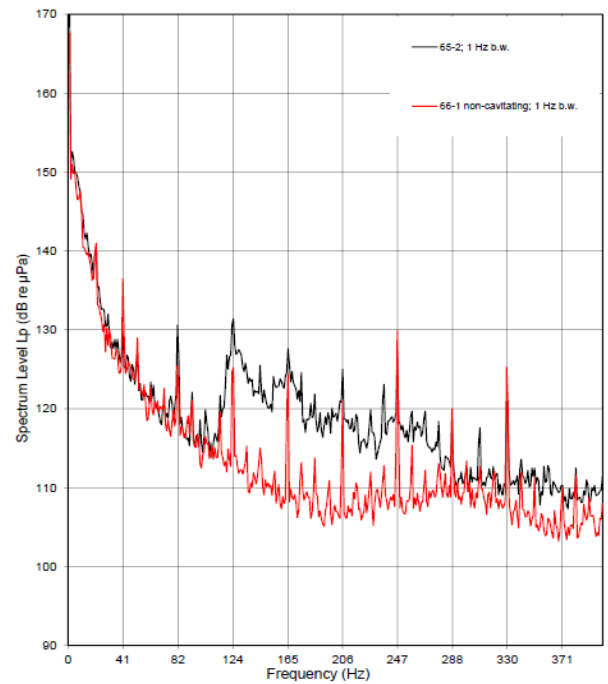
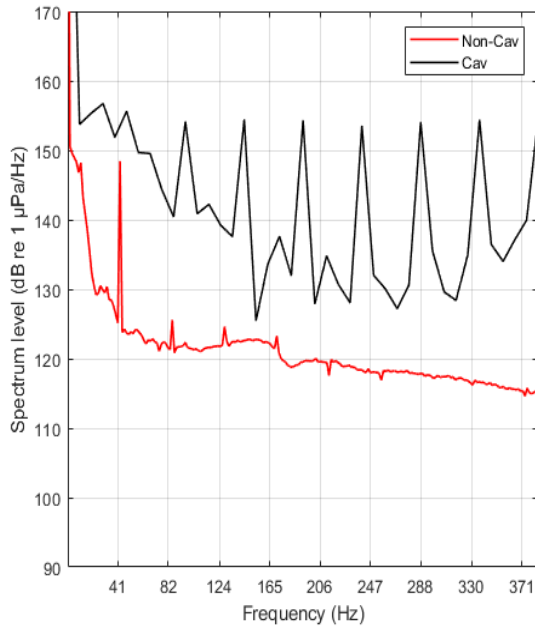


Figure A.2: Spectral Analyses Comparison, Probe 3

(a) CFD model scale predicted



(b) Experimental

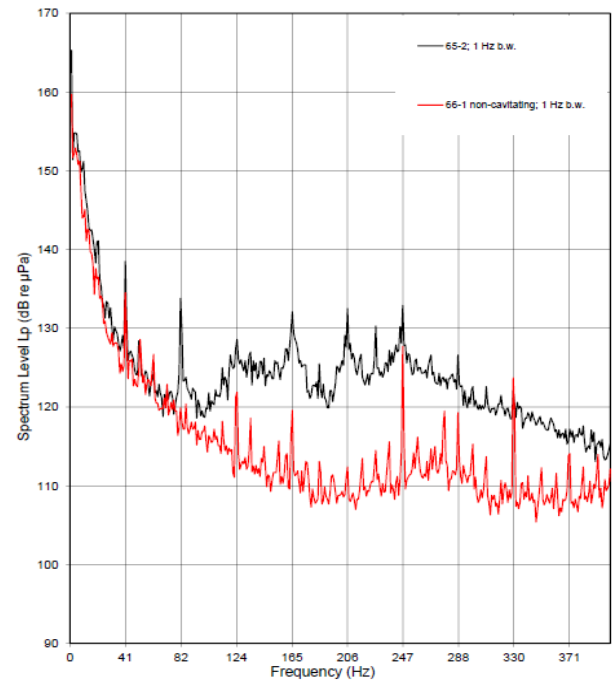
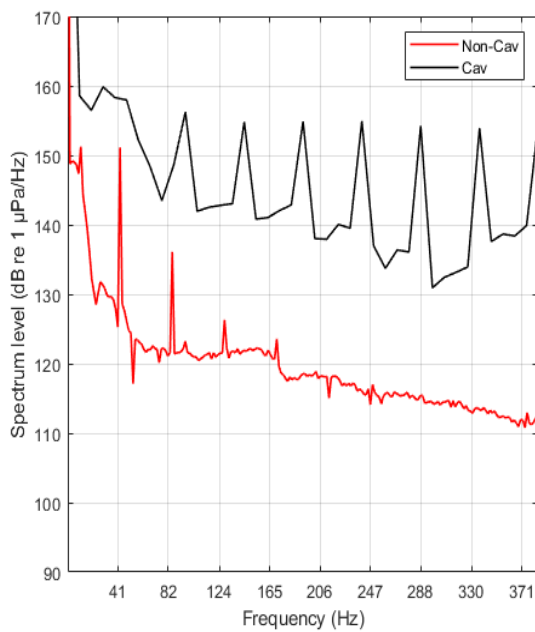


Figure A.3: Spectral Analyses Comparison, Probe 4

(a) CFD model scale predicted



(b) Experimental

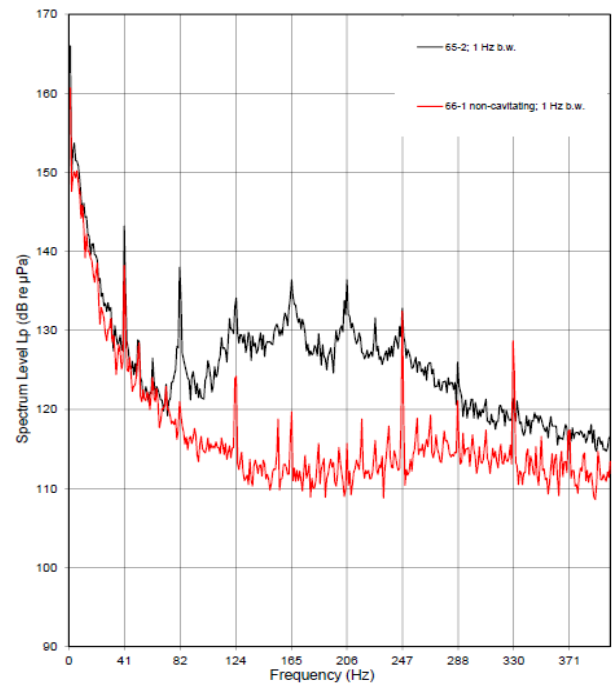
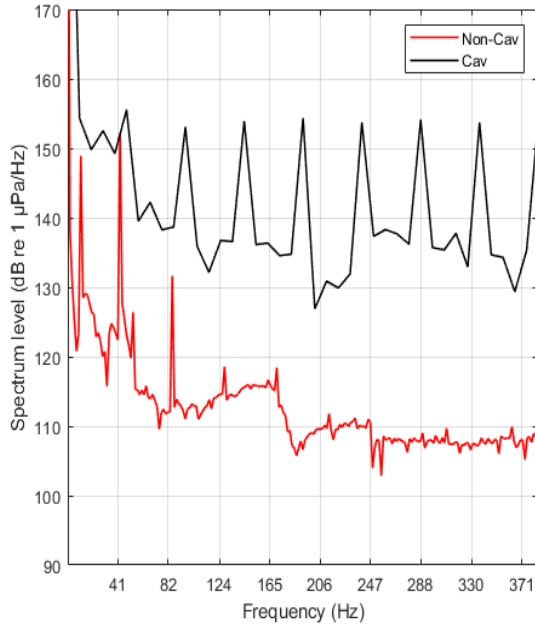


Figure A.4: Spectral Analyses Comparison, Probe 5

(a) CFD model scale predicted



(b) Experimental

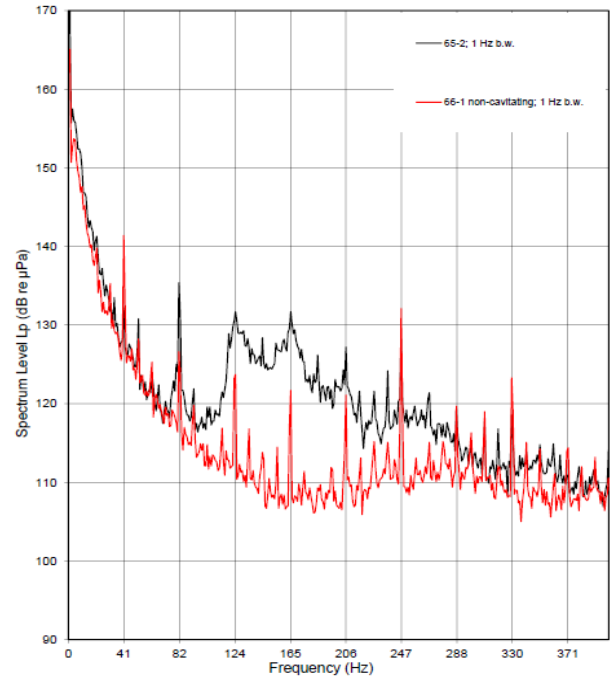
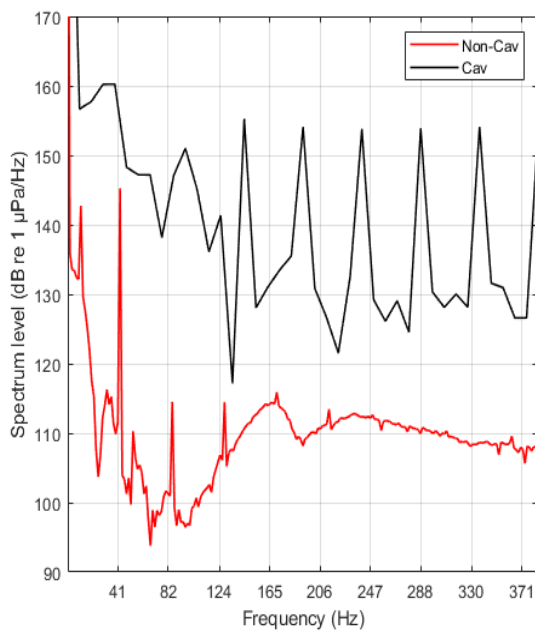


Figure A.5: Spectral Analyses Comparison, Probe 6

(a) CFD model scale predicted



(b) Experimental

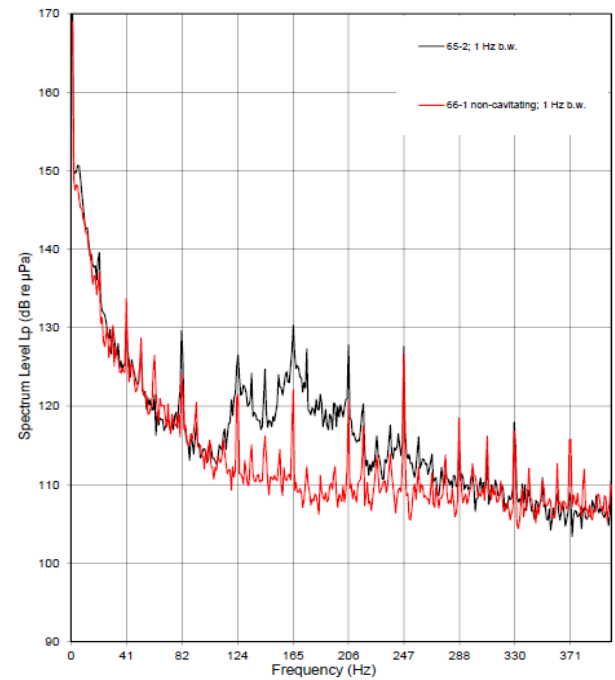
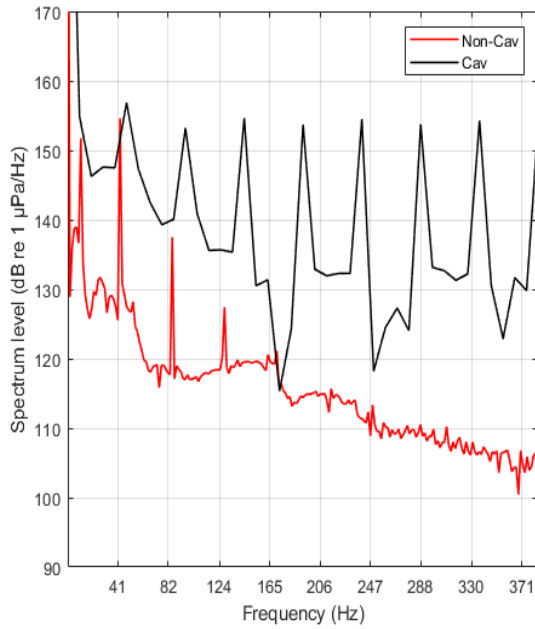


Figure A.6: Spectral Analyses Comparison, Probe 7

(a) CFD model scale predicted



(b) Experimental

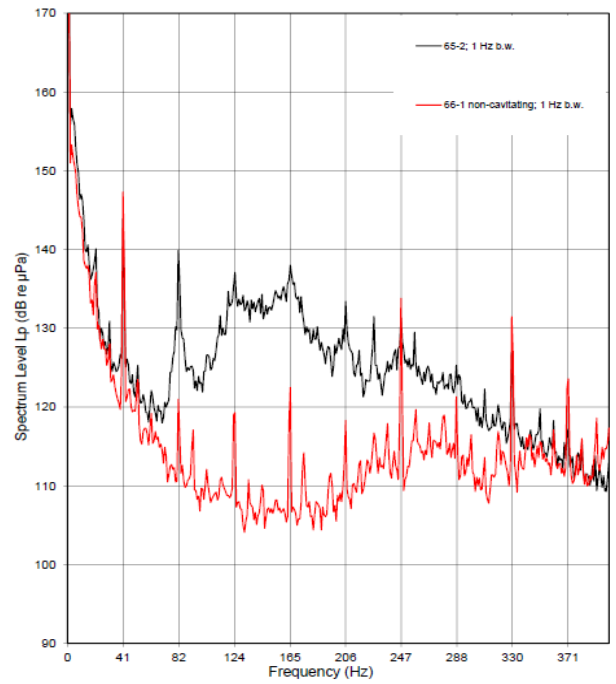
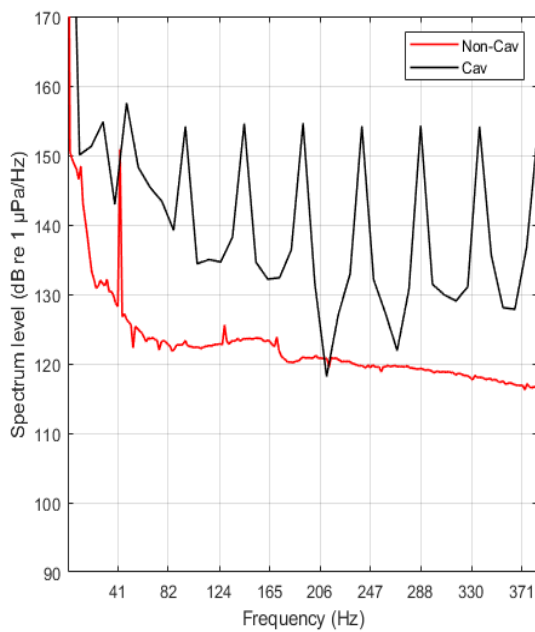


Figure A.7: Spectral Analyses Comparison, Probe 8

(a) CFD model scale predicted



(b) Experimental

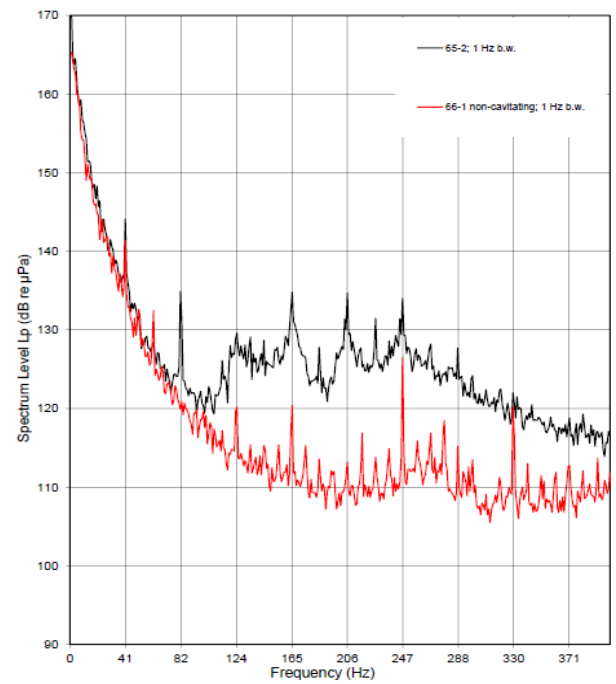
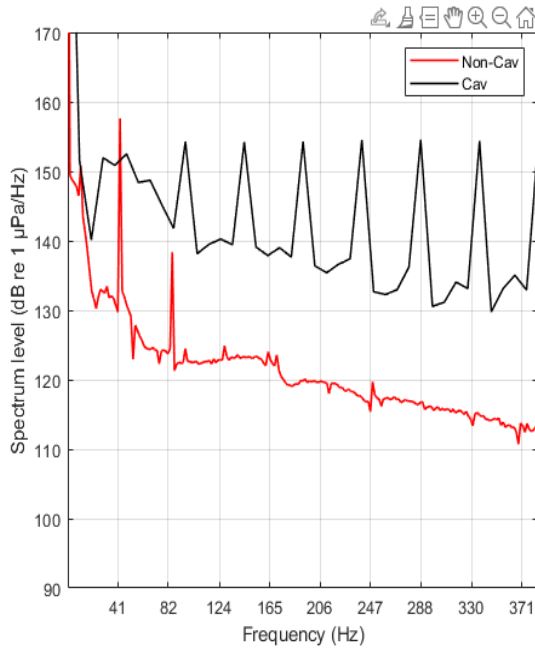


Figure A.8: Spectral Analyses Comparison, Probe 9

(a) CFD model scale predicted



(b) Experimental

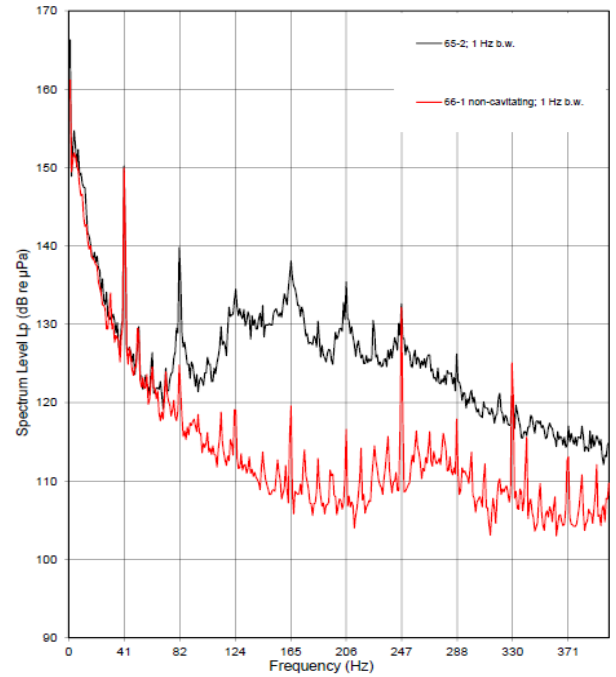
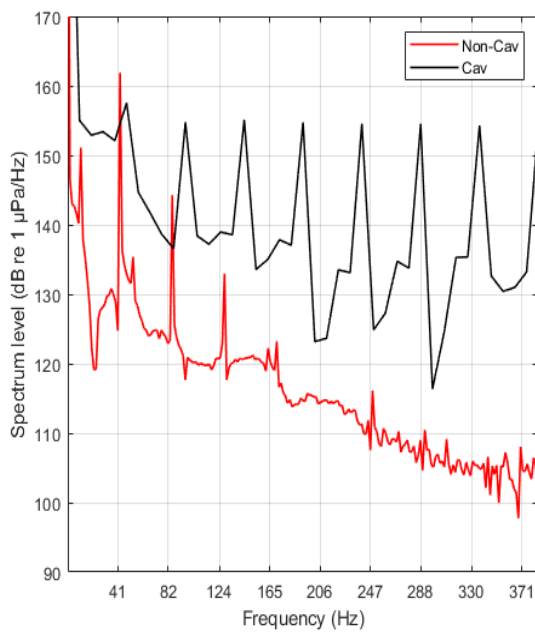


Figure A.9: Spectral Analyses Comparison, Probe 10

(a) CFD model scale predicted



(b) Experimental

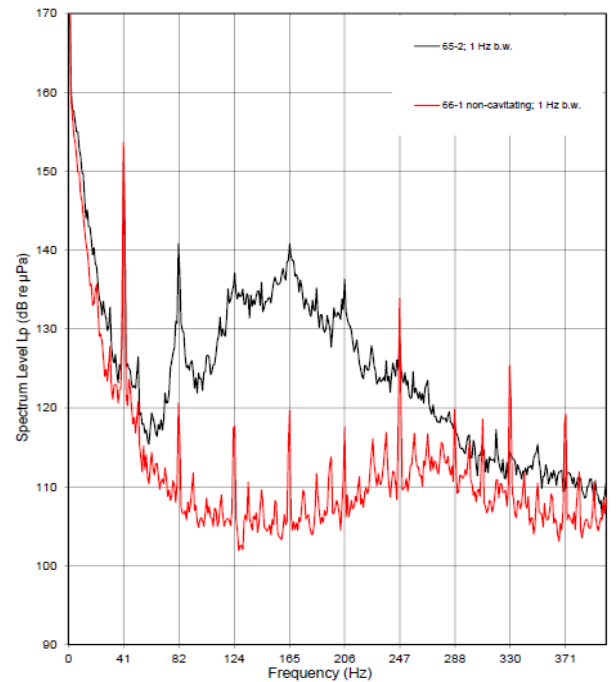
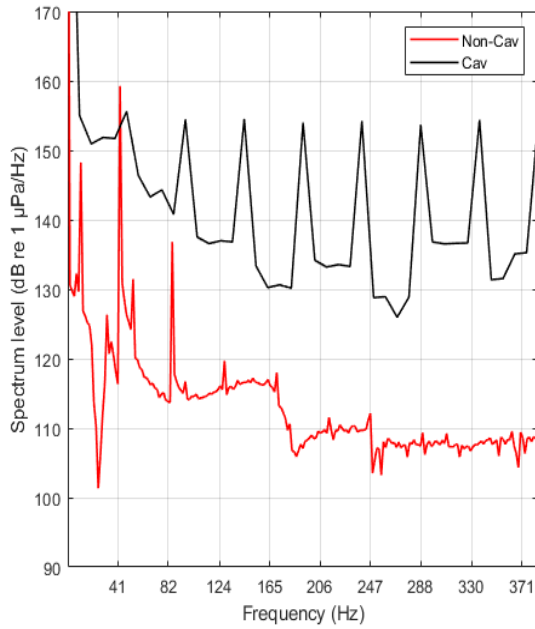


Figure A.10: Spectral Analyses Comparison, Probe 11

(a) CFD model scale predicted



(b) Experimental

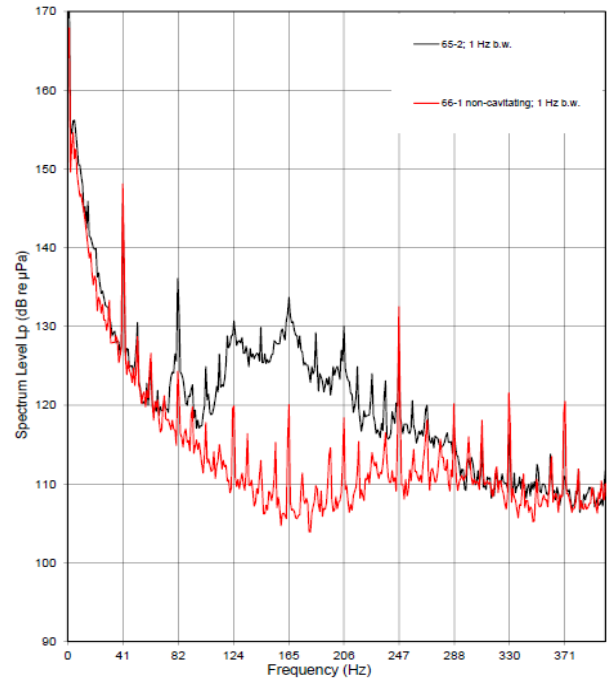
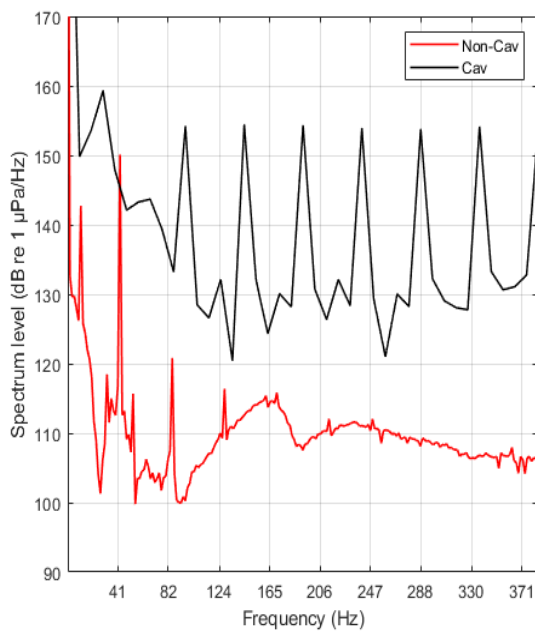


Figure A.11: Spectral Analyses Comparison, Probe 12

(a) CFD model scale predicted



(b) Experimental

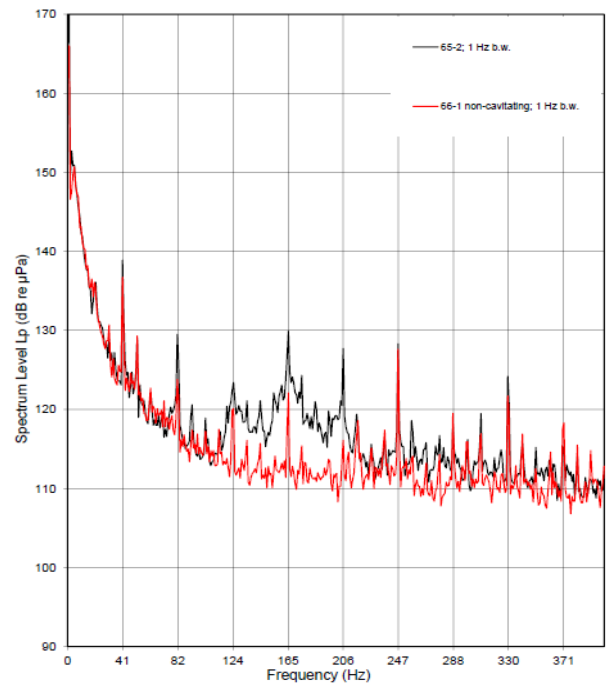
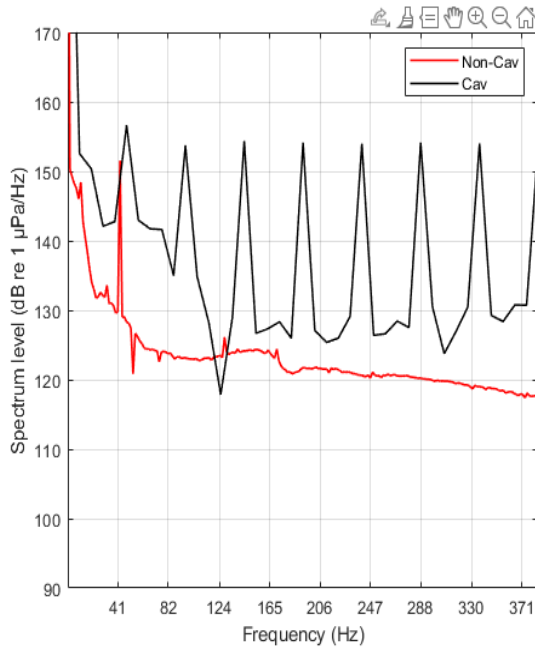


Figure A.12: Spectral Analyses Comparison, Probe 13

(a) CFD model scale predicted



(b) Experimental

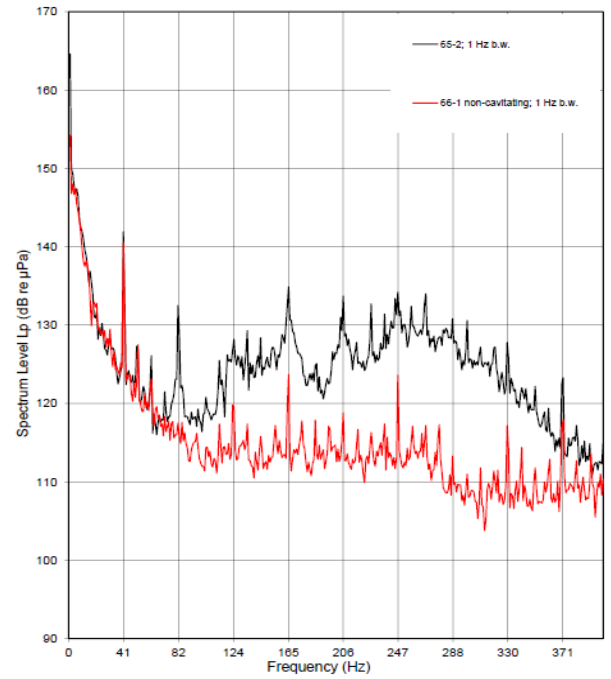
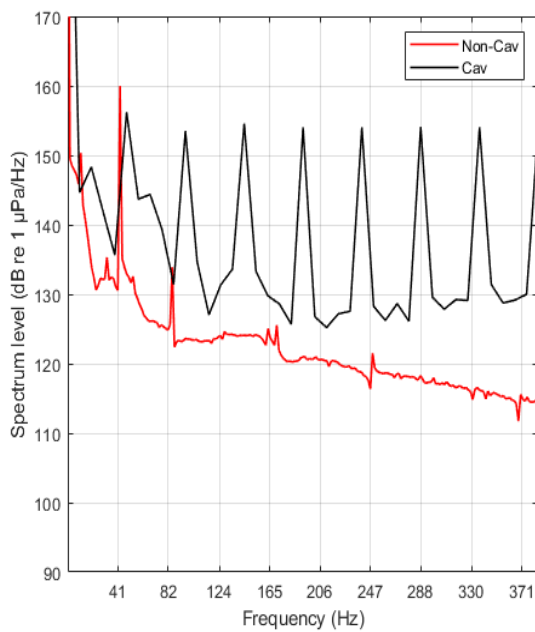


Figure A.13: Spectral Analyses Comparison, Probe 14

(a) CFD model scale predicted



(b) Experimental

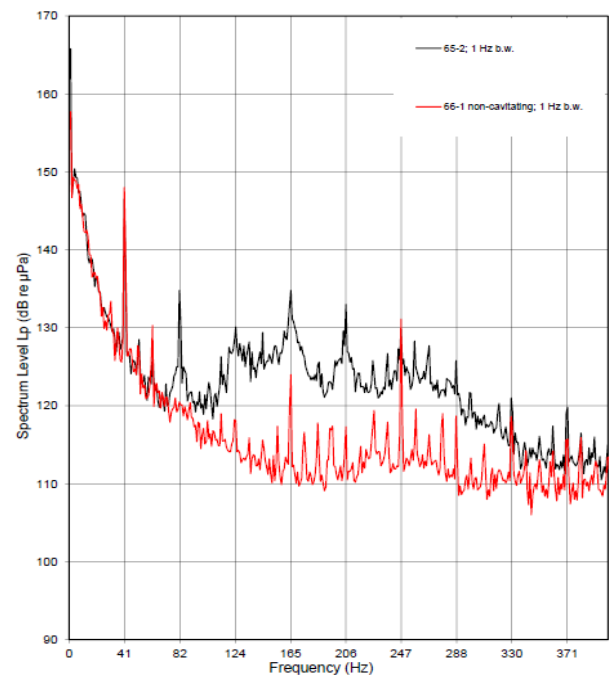
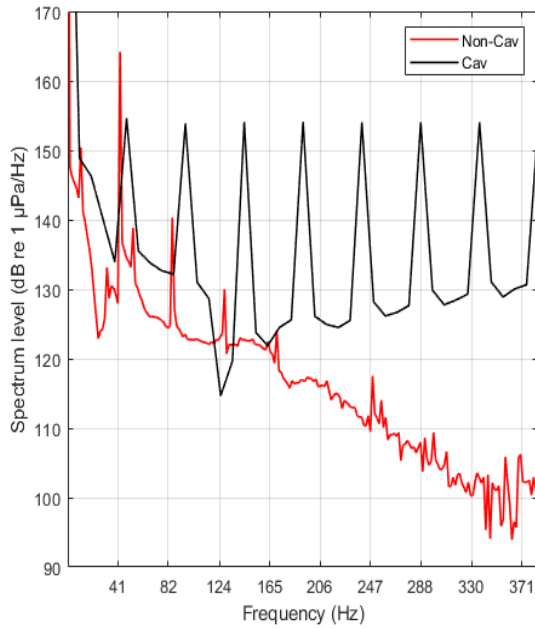


Figure A.14: Spectral Analyses Comparison, Probe 15

(a) CFD model scale predicted



(b) Experimental

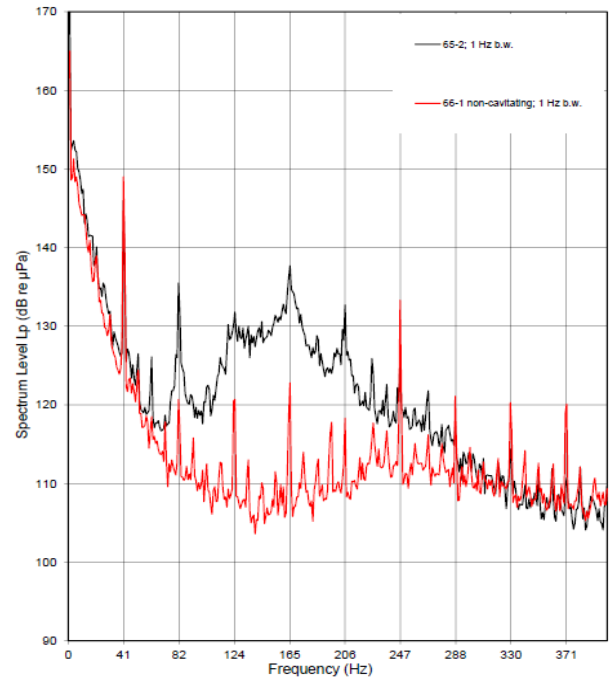
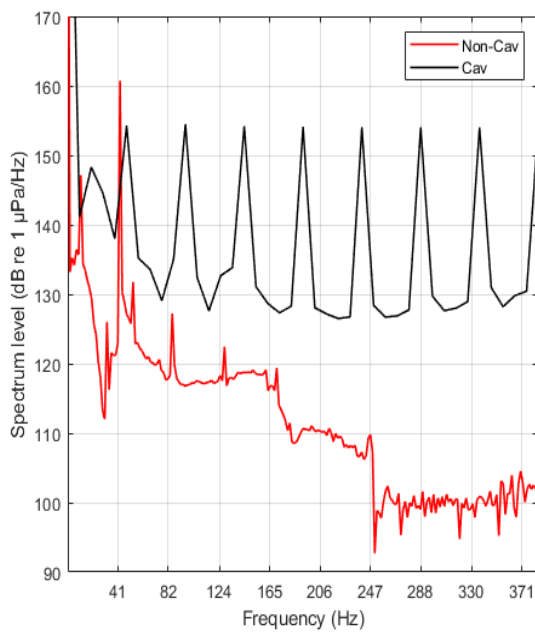


Figure A.15: Spectral Analyses Comparison, Probe 16

(a) CFD model scale predicted



(b) Experimental

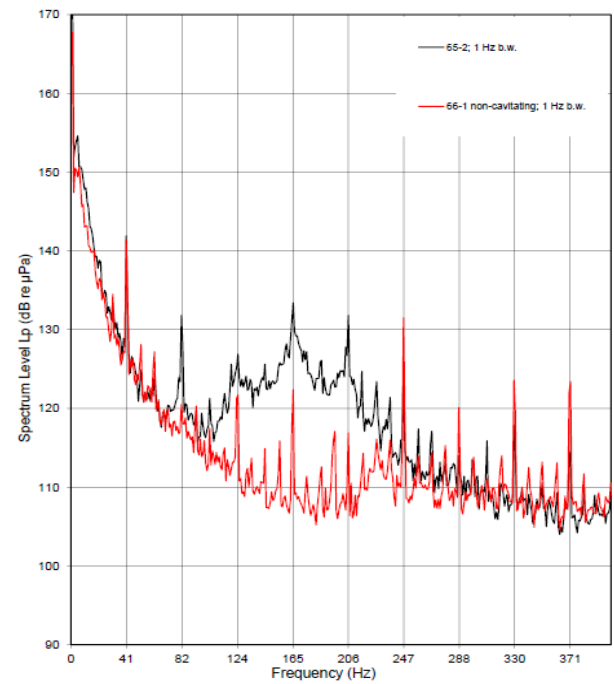
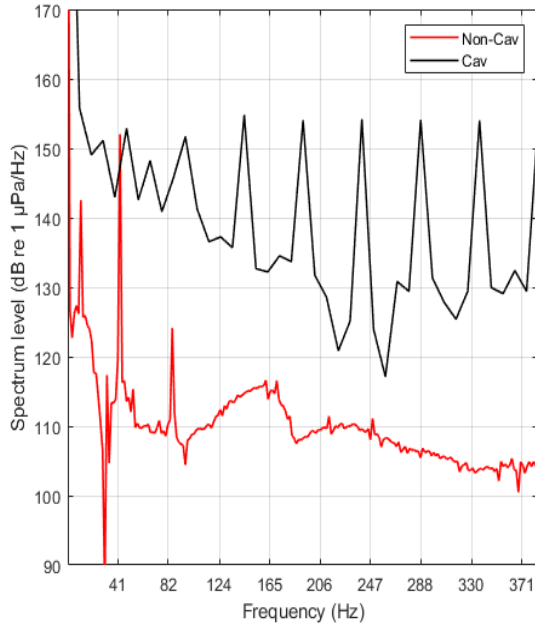


Figure A.16: Spectral Analyses Comparison, Probe 17

(a) CFD model scale predicted



(b) Experimental

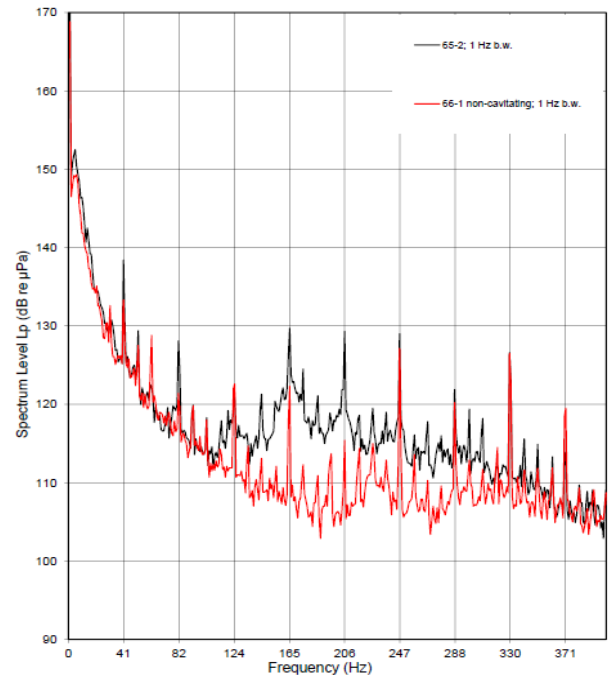
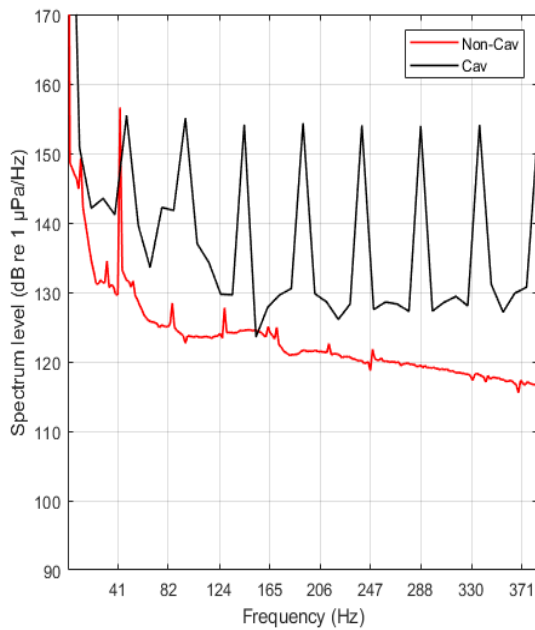


Figure A.17: Spectral Analyses Comparison, Probe 18

(a) CFD model scale predicted



(b) Experimental

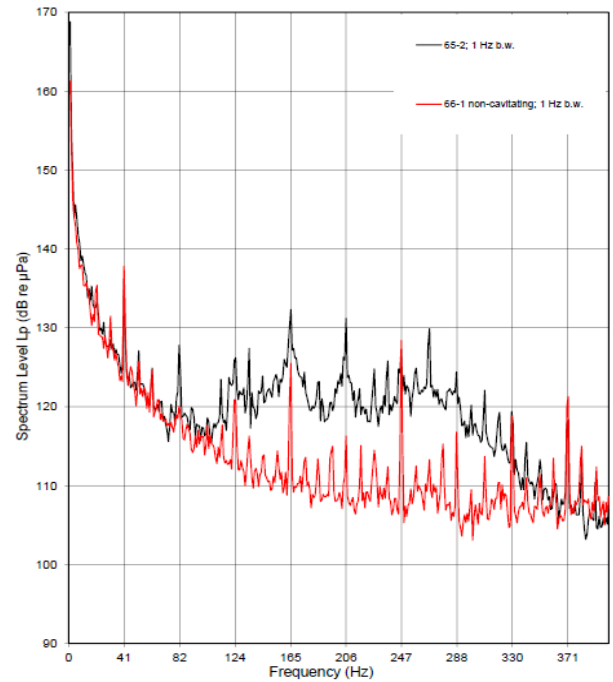
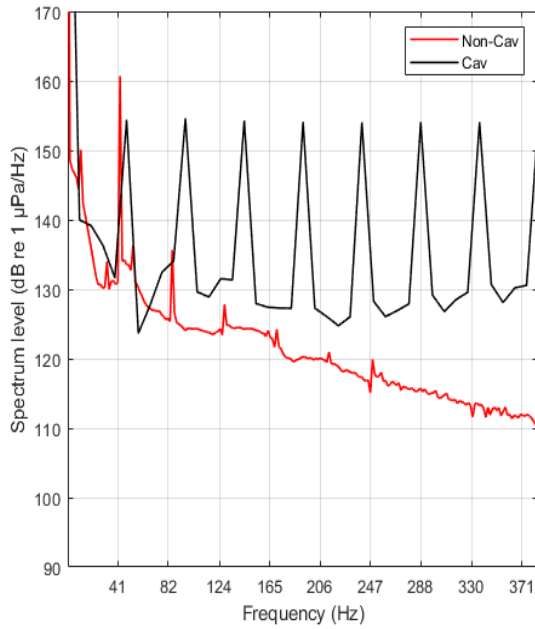


Figure A.18: Spectral Analyses Comparison, Probe 19

(a) CFD model scale predicted



(b) Experimental

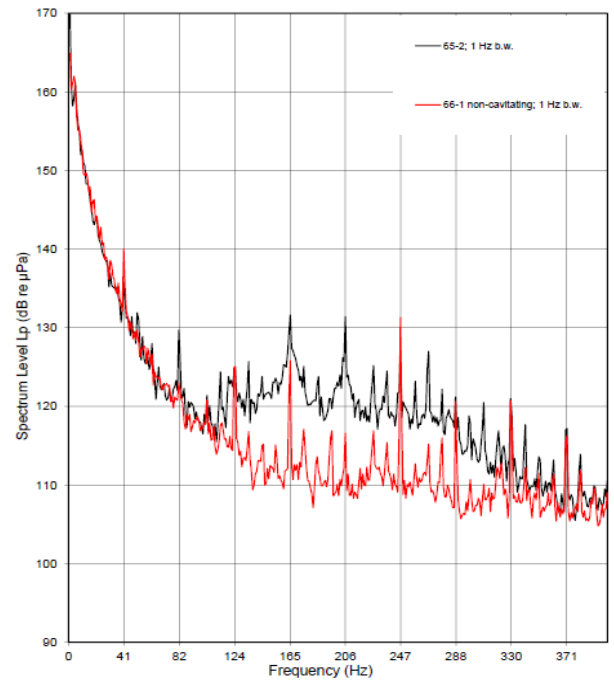
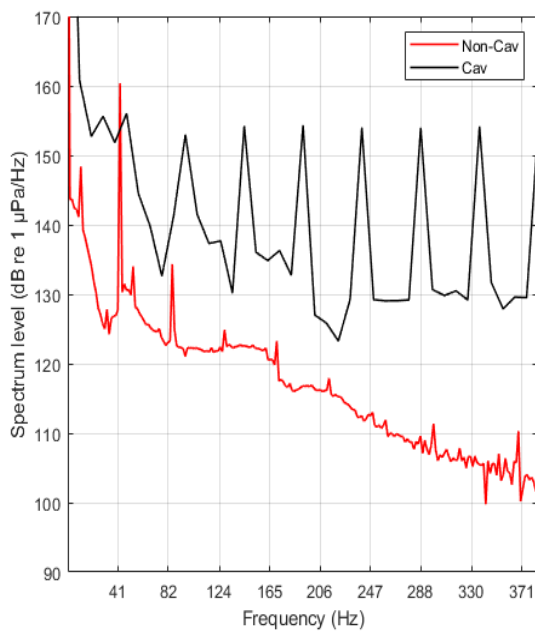


Figure A.19: Spectral Analyses Comparison, Probe 20

(a) CFD model scale predicted



(b) Experimental

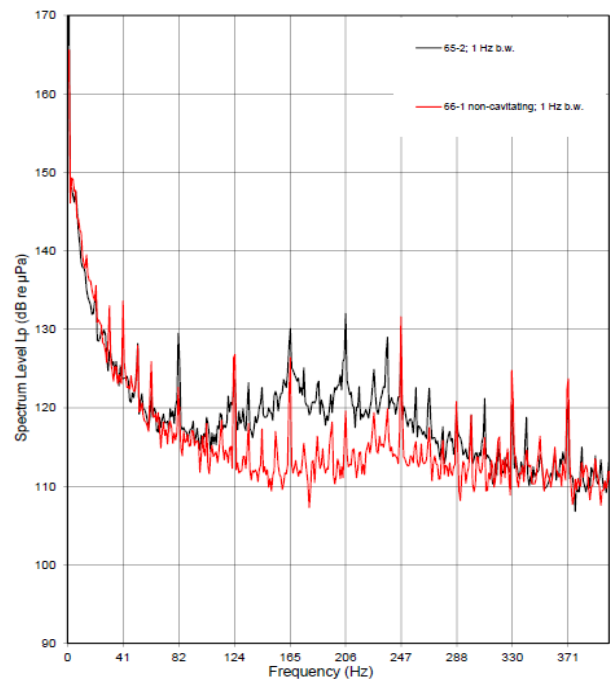
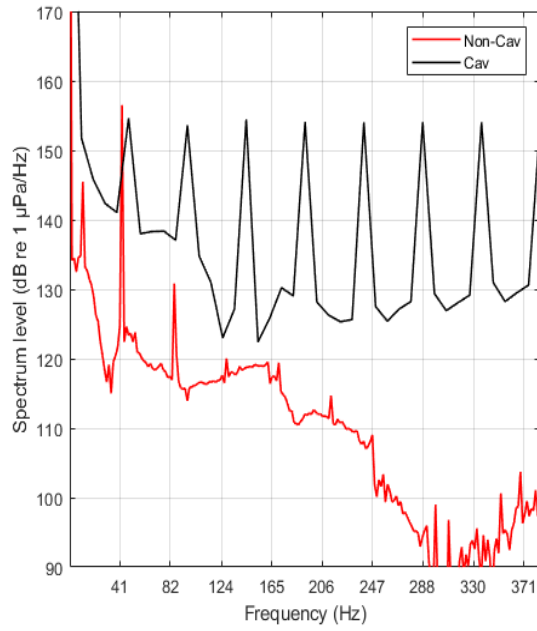
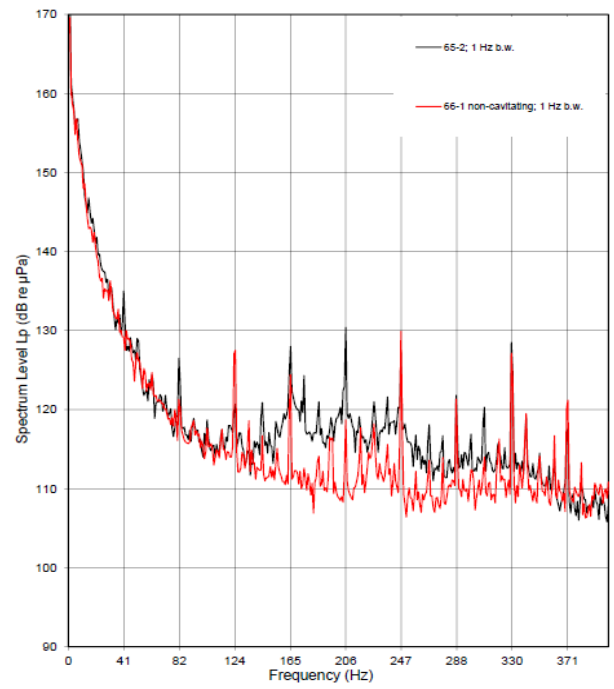


Figure A.20: Spectral Analyses Comparison, Probe 21

(a) CFD model scale predicted



(b) Experimental



DEPARTMENT OF MECHANICS AND MARITIME SCIENCES
CHALMERS UNIVERSITY OF TECHNOLOGY
Gothenburg, Sweden
www.chalmers.se



CHALMERS
UNIVERSITY OF TECHNOLOGY